

Proposal for measuring out-of-time-ordered correlators at finite temperature with coupled spin chains

Bhuvanesh Sundar^{1,2,3}, Andreas Elben^{3,4,5}, Lata Kh Joshi^{3,4}, and Torsten V. Zache^{3,4}

¹JILA, Department of Physics, University of Colorado, Boulder, CO 80309, USA

²Center for Theory of Quantum Matter, University of Colorado, Boulder, CO 80309, USA

³Institute for Quantum Optics and Quantum Information of the Austrian Academy of Sciences, Innsbruck A-6020, Austria

E-mail: bhuvanesh.sundar@colorado.edu

⁴Center for Quantum Physics, University of Innsbruck, Innsbruck A-6020, Austria

⁵Institute for Quantum Information and Matter and Walter Burke Institute for Theoretical Physics, California Institute of Technology, Pasadena, CA 91125, USA

Abstract. Information scrambling, which is the spread of local information through a system's many-body degrees of freedom, is an intrinsic feature of many-body dynamics. In quantum systems, the out-of-time-ordered correlator (OTOC) quantifies information scrambling. Motivated by experiments that have measured the OTOC at infinite temperature and a theory proposal to measure the OTOC at finite temperature using the thermofield double state, we describe a protocol to measure the OTOC in a finite temperature spin chain that is realized approximately as one half of the ground state of two moderately-sized coupled spin chains. We consider a spin Hamiltonian with particle-hole symmetry, for which we show that the OTOC can be measured without needing sign-reversal of the Hamiltonian. We describe a protocol to mitigate errors in the estimated OTOC, arising from the finite approximation of the system to the thermofield double state. We show that our protocol is also robust to main sources of decoherence in experiments.

1. Introduction

Present day quantum simulators based on trapped ions [1, 2], ultracold ground state atoms [3] and Rydberg atoms [4], and other platforms [5–8] provide unique opportunities to study the time evolution of quantum many-body systems in a controlled laboratory setting. In atomic physics, analog quantum simulators with ultracold atoms in deep optical lattices realize effective spin models with nearest-neighbor interactions [3, 9–12], and simulators with Rydberg tweezer arrays or trapped ion chains realize spin models with longer ranged interactions [13–17]. These experiments have several control parameters which allow one to controllably modify, or even completely turn off,

these interactions, for example by increasing the lattice depth in optical lattices or detuning the atomic levels in Rydberg systems. This flexibility, and the ability to imprint local operations and make measurements, pave the way to develop quantum algorithms for measuring quantitative probes of the system's non-equilibrium dynamics and thermalization.

A fundamental question in out-of-equilibrium many-body dynamics is how quantum systems thermalize and scramble information. We describe a protocol to measure a system's finite-temperature out-of-time-ordered correlation (OTOC), which quantifies the nature of information scrambling, and which we will further describe in detail below. Our method is geared towards analog quantum simulators which realize particle-hole symmetric Hamiltonians that satisfy the eigenstate thermalization hypothesis (ETH). The former condition of particle-hole symmetry provides a favorable scenario to simplify the dynamics in our protocol, specifically the backward time evolution in one of the spin chains which is usually challenging to implement, but is not strictly necessary. The latter condition of ETH provides a favorable scenario to approximately prepare the thermofield double (TFD) state [18, 19] that is required as the initial state in our protocol, but has not been shown to be a necessary condition for preparing the TFD. As a concrete example, we consider a long-ranged XX model that can be implemented with Rydberg atoms.

Information scrambling, which is the spread of local information through a system's degrees of freedom, is an intrinsic feature of many-body dynamics [20]. In quantum systems, the effects of scrambling on an initially local operator V are reflected in the Heisenberg time evolution with an underlying Hamiltonian H , i.e., $V(t) = \exp(iHt/\hbar)V(0)\exp(-iHt/\hbar)$. One way to quantify this spread is through the square of the commutator of $V(t)$ with another local operator $W(0)$, i.e., $C(t) = \langle |[V(t), W(0)]|^2 \rangle$. Here, the expectation value is taken in the thermal state $\rho_\beta = \exp(-\beta H)/Z$, with $Z = \text{tr}(\exp(-\beta H))$ and β denotes the inverse temperature, $\beta = 1/(k_B T)$. OTOCs, which we are interested in, are two of the four terms in the expansion of $C(t)$, namely $\langle W^\dagger(0)V^\dagger(t)W(0)V(t) \rangle$ and $\langle V^\dagger(t)W^\dagger(0)V(t)W(0) \rangle$.

The OTOC serves as a crucial observable to understand information scrambling in quantum systems [20–40]. Generically, OTOCs decay with time until $V(t)$ has reached all the degrees of freedom, in a time scale known as the scrambling time, t_{scr} . The scaling of t_{scr} with system size diagnoses how fast or slow the system scrambles information. The decay time and nature of spreading (e.g., diffusive or ballistic) can depend on parameters in the Hamiltonian [32–34, 41–43] or state properties like the temperature (T) [44–46]. In addition to characterizing the nature of scrambling, OTOCs can also be used to diagnose quantum phase transitions [47–55]. Due to their fundamental importance in information scrambling and other applications listed above, there has been enormous interest in measuring OTOCs in recent years.

There are previous theoretical proposals to experimentally measure OTOCs at infinite temperature [37, 56, 57]. Some of them involve time evolution by reversing the Hamiltonian's sign [58], or by controlling the Hamiltonian's sign with an ancillary qubit

which acts as a switch [59, 60]. Proposals to measure OTOCs without reversing time evolution involve implementing the SWAP operator between two systems either as an ensemble of random initial states [56] or in the measurement [61], or by making weak measurements [62, 63]. These methods have been used in experiments to measure the OTOC in nuclear magnetic resonance simulators [64–66], ultracold atoms [67], trapped ions [68–70] and superconducting circuits [71–74].

Refs. [56, 57] describe how to extend the infinite-temperature methods discussed there to measure the OTOC at finite temperature (referred to as thermal OTOC). Other proposals to measure the thermal OTOC consider two copies of the same system in an entangled initial state prepared at a negative time [75], or two copies of the system sampled from a thermal ensemble [61]. However, despite these proposals, the OTOC at a finite temperature has not been measured in experiments.

In this work, we describe how to measure the thermal OTOC in analog quantum simulators, without initial state preparation at negative times or the need to evolve backward in time for systems with particle-hole symmetry. Our method is inspired by ideas to prepare the TFD for systems that satisfy ETH [18, 19], and measure the thermal OTOC from the TFD [19, 75]. Our main contribution is to demonstrate a feasible method to measure a thermal OTOC in current quantum simulators. We illustrate this by using a concrete example, a 1D spin model with long-ranged XX interactions, and showing that one can prepare the thermofield double state with reasonable fidelity at modest system sizes, and measure a thermal OTOC by quenching this state. In this context, we propose a method that obtains a good estimate for the OTOC even in the presence of limitations due to dissipative dynamics and systematic limitations of our protocol. We note that the Hamiltonian we consider was recently realized in experiment [13].

This article is organized as follows. In Section 2, we review the TFD state and show how it can be used to measure thermal OTOCs. In Section 3, we numerically show how to approximately access the TFD for a 1D spin Hamiltonian as the ground state of a local parent Hamiltonian on two coupled spin chains. In Section 4, we numerically show that an approximation to the OTOC can be measured from the ground state described in Section 3, and describe a correction protocol to mitigate the error in this approximation. In Section 5, we numerically show that our correction protocol also mitigates errors that arise from decoherence in experiment. In Section 6, we discuss connections between our protocol and previous proposals to measure the OTOC. We summarize in Section 7.

2. O_{th} from Thermofield Double state

There are different regularized versions of the thermal OTOC in the literature [25, 61, 75]. Here, we consider the following thermal OTOC between operators W and V ,

$$O_{th}(\beta, t) = \frac{\text{tr} \left(e^{-\beta H/2} W^\dagger V^\dagger(t) W e^{-\beta H/2} V(t) \right)}{Z}. \quad (1)$$

In Appendix A, we state the other definitions of the thermal OTOC and explore their temperature dependence for the model considered in this paper.

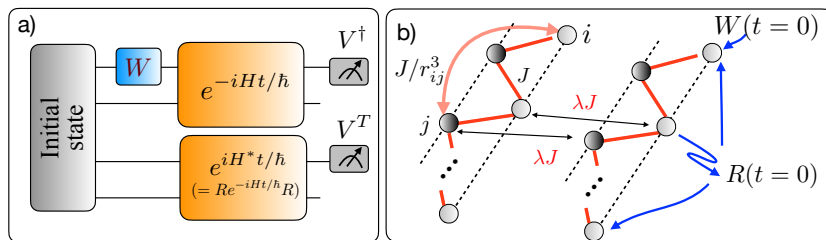


Figure 1. (a) Schematic of the protocol to measure the OTOC. We propose to initialize the system in the thermofield double state $|\text{tfd}(\beta)\rangle$ in the exact protocol, and in the ground state $|g(\lambda)\rangle$ of H_{parent} in the experimentally feasible protocol, which closely approximates $|\text{tfd}(\beta)\rangle$ up to a symmetry operation (see main text). Then, we apply $W \otimes 1$, and evolve the two halves independently with H and $-H^*$ respectively. For the example we consider [see (b)], $-H^* = RHR$ can be realized by implementing unitary single-qubit gates R before and after time evolution with H . Measuring $V^\dagger \otimes V^T$ gives O_{th} in the exact protocol, and $O_g \sim O_{\text{th}}$ in the experimental case [see (12)]. Performing an identical experiment with $W = 1$ gives N_g . The corrected estimate for the OTOC is $O_{\text{corr}} = O_g/N_g$ [(13)]. (b) Schematic of the physical setup. We consider qubits on a $2 \times n$ ladder, with long-range intra-leg interactions given by J/r_{ij}^3 [see (6)], and inter-leg interactions given by λJ [(10)] which sets the effective temperature. The intra-leg Hamiltonian was recently realized in [13]. The initial state is prepared at $t = 0$, the inter-leg coupling λ is turned off and $W \otimes R$ is applied at $t = 0$, and the two legs are evolved independently for $t > 0$.

The TFD state at temperature $T \equiv 1/(k_B\beta)$ is an entangled state on $2n$ qubits (for an n -qubit Hamiltonian), defined as

$$|\text{tfd}(\beta)\rangle = \frac{\sum_E e^{-\beta E/2} |E\rangle \otimes |E^*\rangle}{\sqrt{Z}}. \quad (2)$$

The sum in (2) runs over the eigenstates $|E\rangle$ of H , with respective eigenvalues E , i.e., $H|E\rangle = E|E\rangle$. We denote H^* and $|E^*\rangle$ as the complex conjugates of H and $|E\rangle$, satisfying $H^*|E^*\rangle = E|E^*\rangle$. Preparing $|\text{tfd}(\beta)\rangle$, which is a highly entangled state, in an experiment is non-trivial and is an active area of research. One technique that has been successfully used in the past uses variational quantum circuits [76, 77]. Here, we show that O_{th} can be measured if one can access $|\text{tfd}(\beta)\rangle$.

In an ideal situation where an experiment can access $|\text{tfd}(\beta)\rangle$, Figure 1(a) shows a circuit for measuring $O_{\text{th}}(\beta, t)$. Realizing the circuit assumes that W is a unitary operator, so that it can be applied in the circuit, and V is Hermitian, so that it can be measured at the end. After preparing the initial state $|\text{tfd}(\beta)\rangle$, the circuit applies $W \otimes 1$. This step prepares $|\psi_W(\beta, 0)\rangle = (W \otimes 1)|\text{tfd}(\beta)\rangle$. We then evolve the system with $H \otimes 1 - 1 \otimes H^*$ for a time t , and measure $V^\dagger \otimes V^T$, leading to,

$$O_{\text{tfd}}(\beta, t) = \langle \psi_W(\beta, t) | V^\dagger \otimes V^T | \psi_W(\beta, t) \rangle. \quad (3)$$

Here, $|\psi_W(\beta, t)\rangle = \exp(-i(H_1 - H_2^*)t/\hbar) |\psi_W(\beta, 0)\rangle$, where we denote $H_1 = H \otimes 1$ and $H_2 = 1 \otimes H$. This protocol requires evolving qubits $[n+1, 2n]$ with $-H^*$. We remark that such backward time evolution is a generic feature of protocols that measure the

OTOC, except for specific protocols designed to measure the OTOC with only forward time evolution [56, 69].

The measurement $O_{\text{tfd}}(\beta, t)$ in (3) is equal to the thermal OTOC $O_{\text{th}}(\beta, t)$ in (1). This can be seen from

$$\begin{aligned}
 O_{\text{tfd}}(\beta, t) &= \langle \text{tfd}(\beta) | (W^\dagger \otimes 1) e^{i(H_1 - H_2^*)t/\hbar} (V^\dagger \otimes V^T) e^{-i(H_1 - H_2^*)t/\hbar} (W \otimes 1) | \text{tfd}(\beta) \rangle \\
 &= \sum_{EE'} \frac{e^{-\beta(E+E')/2}}{\text{tr } e^{-\beta H}} \langle E' | W^\dagger e^{iHt/\hbar} V^\dagger e^{-iHt/\hbar} W | E \rangle \langle E'^* | e^{-iH^*t/\hbar} V^T e^{iH^*t/\hbar} | E^* \rangle \\
 &= \sum_{EE'} \frac{e^{-\beta(E+E')/2}}{\text{tr } e^{-\beta H}} \langle E' | W^\dagger e^{iHt/\hbar} V^\dagger e^{-iHt/\hbar} W | E \rangle \langle E | e^{iHt/\hbar} V e^{-iHt/\hbar} | E' \rangle \\
 &= \frac{\text{tr} (e^{-\beta H/2} W^\dagger V^\dagger(t) W e^{-\beta H/2} V(t))}{\text{tr } e^{-\beta H}} \\
 &= O_{\text{th}}(\beta, t).
 \end{aligned} \tag{4}$$

The second line of (4) is obtained by inserting the definition of $|\text{tfd}(\beta)\rangle$. Using the general relations $\langle E'^* | O^* | E^* \rangle = \langle E' | O | E \rangle^* = \langle E | O^\dagger | E' \rangle$ for any operator O , we obtain the third line of (4) by setting $O = \exp(iHt/\hbar) V^\dagger \exp(-iHt/\hbar) = V^\dagger(t)$, and noting $(V^\dagger)^* = V^T$. The fourth line is obtained from the identity $\sum_E \exp(-\beta E/2) |E\rangle \langle E| = \exp(-\beta H/2)$ and the cyclic property of the trace.

A corollary of (4) is that setting $W = 1$ yields a measurement that is constant in time. This is because $|\text{tfd}(\beta)\rangle$ is an eigenstate of $H_1 - H_2^*$. We denote this special case as $N_{\text{tfd}}(\beta)$,

$$\begin{aligned}
 N_{\text{tfd}}(\beta) &= \langle \psi_{W=1}(\beta, t) | V^\dagger \otimes V^T | \psi_{W=1}(\beta, t) \rangle \\
 &= \frac{\text{tr} (e^{-\beta H/2} V^\dagger e^{-\beta H/2} V)}{\text{tr } e^{-\beta H}}.
 \end{aligned} \tag{5}$$

Note, $N_{\text{tfd}}(\beta) = O_{\text{tfd}}(\beta, t = 0) \leq 1$. This is unlike some of the other regularizations, where the initial value of the OTOC is 1 [see Appendix Appendix A]. We plot $O_{\text{tfd}}(\beta, t = 0)$ versus temperature in Appendix Appendix A.

Next, we present a protocol suitable for analog quantum simulators, inspired by earlier findings in [18, 19, 75], where we approximately realize $|\text{tfd}(\beta)\rangle$ via the ground state of a local parent Hamiltonian.

3. Approximating $|\text{tfd}(\beta)\rangle$ in an atomic quantum simulator

For a certain class of Hamiltonians – those that satisfy the eigenstate thermalization hypothesis (ETH) – the TFD state has a large overlap with the ground state of a local parent Hamiltonian defined on two appropriately coupled copies of the system [18]. We consider the Hamiltonian on a single 1D chain to be

$$H = \sum_i \sum_{j \text{ odd}} \frac{J}{r_{ij}^3} (\sigma_i^x \sigma_j^x + \sigma_i^y \sigma_j^y) \tag{6}$$

where r_{ij} is the distance between spins i and j , J is the interaction strength between neighboring spins, and the sum runs over $1 \leq i, j \leq n$ with i odd and j even. We

expect that the long-range interactions will allow the system to thermalize and thus satisfy ETH. Consistent with this, we will show analytical and numerical evidence that the ground state of a local parent Hamiltonian has a large overlap with the TFD state for moderate system sizes $n \leq 11$. We remark that we do not explicitly verify or use the fact that (6) satisfies ETH, but merely use the arguments put forth by earlier works [18] as a motivation to obtain the TFD as the ground state of a parent Hamiltonian. There are other approaches to prepare the TFD as well, e.g. using variational quantum circuits [76, 77].

We chose the above Hamiltonian H for two further reasons. First, a recent experiment [13] with Rydberg atoms has realized a variant of H where the nearest-neighbor interactions are staggered, i.e. a long-range SSH model, by arranging the atoms in a tilted ladder geometry. Realizing the necessary parent Hamiltonian in our protocol [see following sections] could be achieved by placing two such tilted ladders on nearby planes, as shown in Figure 1(b). The second reason is that the Hamiltonian we consider has particle-hole symmetry, which makes it straightforward to realize the time evolution with $-H^*$ in experiment, which is necessary in our protocol [see Section 2]. Particle-hole symmetry means that there exists a unitary R such that $-H^* = R^\dagger H R$, shown as a parenthetical comment in the time evolution operator in Figure 1(a). For our example, $R = \prod_{n+1 \leq k \leq 2n, k \in \text{even}} \sigma_k^z$ is composed of single-qubit rotations. This is significant because it is easier to realize the evolution operator $\exp(-i(H_1 - H_2^*)t/\hbar)$ as $(1 \otimes R^\dagger) \exp(-i(H_1 + H_2)t/\hbar)(1 \otimes R)$ than by physically reversing the sign of the interactions, where we denote $H_1 = H \otimes 1$ and $H_2 = 1 \otimes H_2$. The idea to reverse 1D spin Hamiltonians using single-qubit rotations was first put forth in Ref. [37]. Some particle-hole symmetric models have relatively simple forms for R . For example, the nearest-neighbor transverse Ising model has $R_{\text{TIM}} = (\prod_{i \text{ odd}} \sigma_i^x)(\prod_{i \text{ even}} \sigma_i^z)$. However, finding and implementing such R may be infeasible for other cases. We note that particle-hole symmetry is not a requirement; depending on the experimental setup, it may be advantageous to explicitly reverse the Hamiltonian's sign in experiment.

3.1. Parent Hamiltonian: Special cases

Let us begin by finding the parent Hamiltonian for $|\text{tfd}(\beta)\rangle$ for a few special cases.

At $\beta = \infty$, $|\text{tfd}(\beta)\rangle$ is a product of the ground state of each spin chain. In this case, $|\text{tfd}(\beta = \infty)\rangle$ is the ground state of

$$H_{\beta=\infty} = H_1 + H_2, \quad (7)$$

where $H_1 = H \otimes 1$ and $H_2 = 1 \otimes H_2$.

At $\beta = 0$, $|\text{tfd}(\beta)\rangle$ is a tensor product of EPR pairs, $(|\uparrow_i \uparrow_{i+n}\rangle + |\downarrow_i \downarrow_{i+n}\rangle)\sqrt{2}$. Each EPR pair is the ground state of $\sigma_i^y \sigma_{i+n}^y - \sigma_i^x \sigma_{i+n}^x$. Based on this, we can write that $|\text{tfd}(\beta = 0)\rangle$ as the ground state of

$$H_{\beta=0} = J \sum_i \sigma_i^y \sigma_{i+n}^y - \sigma_i^x \sigma_{i+n}^x. \quad (8)$$

As a final special case, in Appendix B, we analytically derive the parent Hamiltonian for $|\text{tfd}(\beta)\rangle$ for $n = 2$ at arbitrary temperature, finding that β is uniquely set by λ .

We remark that the form of interactions in (8) are such that they are ferromagnetic in the σ^x direction, and anti-ferromagnetic in the σ^y direction for $J > 0$ (vice versa for $J < 0$), unlike the interactions in H_1 and H_2 where they are anti-ferromagnetic along both directions. Experimentally, it is however more convenient to realize a system where the interactions have the same sign along all directions. For example, dipole interactions give rise to flip-flip interactions, which yield the same sign for interactions along x and y . To overcome this inconvenient scenario, we consider the coupling Hamiltonian

$$H_{12} \equiv SH_{\beta=0}S = J \sum_i \sigma_i^y \sigma_{i+n}^y + \sigma_i^x \sigma_{i+n}^x \quad (9)$$

where $S = \prod_{i=1}^n \sigma_i^y$, and note that the ground state $|\phi(\beta = 0)\rangle$ of H_{12} is related to $|\text{tfd}(\beta = 0)\rangle$ as $|\phi(\beta)\rangle = S |\text{tfd}(\beta)\rangle$. We also note that $|\phi(\beta = \infty)\rangle \equiv S |\text{tfd}(\beta = \infty)\rangle$ is a ground state of $H_1 + H_2$ from (7).

3.2. Parent Hamiltonian: General case

For intermediate temperature, $0 < T < \infty$ (i.e. $0 < \beta < \infty$), we make an ansatz for the parent Hamiltonian,

$$H_{\text{parent}}(\lambda) = H_1 + H_2 + \lambda J \sum_i (\sigma_i^y \sigma_{i+n}^y + \sigma_i^x \sigma_{i+n}^x). \quad (10)$$

We numerically show below that the ground state of this Hamiltonian, $|g(\lambda)\rangle$, has a large fidelity with $|\phi(\beta)\rangle = S |\text{tfd}(\beta)\rangle$, where the fidelity is defined as

$$F(\beta, \lambda) = |\langle g(\lambda) | \phi(\beta) \rangle|^2. \quad (11)$$

It is possible to verify whether (10) is a good ansatz, for each β , by numerically searching for the value of the inter-chain coupling λ that maximizes $F(\beta, \lambda)$. The ansatz is good if $F(\beta, \lambda) \sim 1$. Moreover, we will use $F(\beta, \lambda)$ to put a (loose) bound on the error in the OTOC provided by our protocol. The coupling λ may be tuned in experiments by adjusting the distance between the chains, or their orientation relative to the quantization axis, and the value of λ sets the inverse temperature β realized by the state. Following this intuition, we numerically search for $\beta_0 = \text{argmax}_\beta F(\beta, \lambda)$, for each λ .

3.3. Numerical results for β

Figure 2(a) plots the maximum fidelity $F(\beta_0, \lambda) = \max_\beta F(\beta, \lambda)$ versus λ , and Figure 2(b) plots the temperature $T_0 = 1/(k_B \beta_0)$ where this maximum occurs. The optimum fidelity is always $\gtrsim 88\%$ up to $n = 11$, and is smallest around $\lambda = 1$ for all n . The inset shows the scaling of $F(\beta_0, \lambda)$ with n at $\lambda = 1$. The temperature T_0 corresponding to the maximum fidelity smoothly increases with λ and varies with n . We extrapolate T_0 to $n = \infty$, by fitting a straight line to T_0 versus $1/n$ as shown in

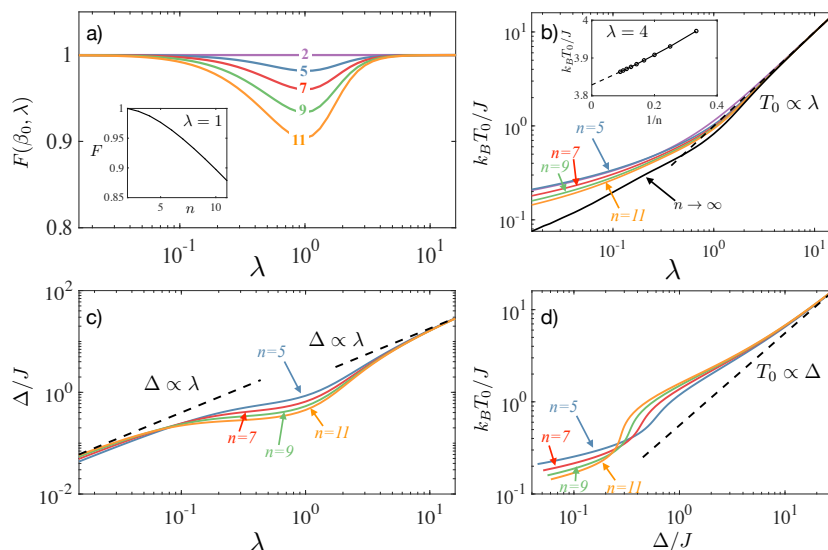


Figure 2. (a) Maximum fidelity $F(\beta_0, \lambda) = \max_{\beta} F(\beta, \lambda)$ versus inter-leg coupling λ . Inset shows $F(\beta_0, \lambda)$ versus n at $\lambda = 1$. $F(\beta_0, \lambda) \gtrsim 0.88$ for $n \leq 11$. (b) Effective temperature T_0 , where the fidelity is maximum, versus inter-leg coupling λ . We extrapolate T_0 to $n \rightarrow \infty$ by doing a linear fit of T_0 versus $1/n$. Inset shows this extrapolation for $\lambda = 4$. (c) The many-body energy gap Δ of H_{parent} versus λ . The gap scales linearly with λ except in a region around $\lambda = 1$. (d) The effective temperature T_0 versus the gap Δ .

the inset of Figure 2(b). Consistent with perturbation theory [78], T_0 increases linearly with λ for $\lambda \gg 1$.

We point out that the fidelity is smallest near $\lambda \sim 1$, and therefore our protocol will perform worse around this region than far away from this region. In Section 4, we will describe a heuristic method to measure the OTOC with reasonable accuracy even when $F(\beta, \lambda)$ deviates from 1.

3.4. Physical intuition for TFD

We give several intuitive arguments for why coupling the two chains as in $H_{\text{parent}}(\lambda)$ gives the TFD, which could be beneficial to readers from different audiences. All of these arguments argue that after tracing out the degrees of freedom in one chain, say the qubits $n + 1 \leq i \leq 2n$, the reduced state ρ_1 is a thermal state of H , which is consistent with having a TFD.

Our first intuitive argument is as follows. Due to the coupling λ between the chains, there is entanglement between the chains, and therefore each chain has a nonzero entanglement entropy. This entanglement entropy, at an intuitive level, makes each chain look like a thermal chain whose temperature is determined by λ . ETH is sufficient, but not strictly necessary, for this intuition to hold. In systems that satisfy ETH, a subsystem (i.e. one chain in our case) looks thermal.

Our second argument uses the language of modular Hamiltonians. The modular Hamiltonian of a subsystem is the Hamiltonian for which the subsystem is a thermal

state, i.e. the reduced density matrix of the subsystem is $\rho = \exp(-H_{\text{modular}})$. Several works [78–81] have shown that H_{modular} of one chain in the many-body ground state on two coupled chains is proportional to the parent Hamiltonian restricted to that chain, i.e. H_1 or H_2 in this case. The observation that $H_{\text{modular}} \propto H_1, H_2$ remarkably appears to hold for a wide variety of lattice models, and was originally motivated by the Bisognano Wichmann theorem or conformal field theory (CFT) [82–85].

Our third argument relies on CFT. In [85], the authors considered two CFTs described by Hamiltonians $H_{1/2}$ and coupled by an interaction λH_{12} , similar to our case, and showed that the reduced state is $\rho_1 \propto e^{-H_1/k_B T}$. They showed that the effective temperature T is proportional to the energy gap Δ , and that $\Delta \propto \lambda$. For comparison, this is consistent with the construction of the TFD in [19]. We expect the low-energy properties of our model to be well described by a CFT, and therefore the reduced states ρ_1 and ρ_2 to be thermal states of H , which is consistent with having a TFD.

Figure 2(c) provides evidence for the CFT explanation above, by plotting the gap Δ versus λ and demonstrating that the approximate relation $\Delta \propto \lambda$ also holds in this case. Note that the fidelity decreases in the region where we observe a deviation from the linear scaling $\Delta \propto \lambda$. For comparison, we also plot T_0 versus Δ in Figure 2(d), and find that $T_0 \propto \Delta$ for large Δ , but it deviates from this linear scaling for $\Delta \lesssim 10J$.

4. Measuring the OTOC from $|g(\lambda)\rangle$

As we showed above, $|g(\lambda)\rangle$ approximates $|\phi(\beta_0)\rangle = S|\text{tfd}(\beta_0)\rangle$. The protocol that we described in Sec. 2 requires the initial state to be $|\text{tfd}(\beta)\rangle = S^\dagger|\phi(\beta)\rangle$, which can be (approximately) prepared easily by applying S^\dagger to the initial state $|\phi(\beta)\rangle$. We will consider W and V as single-qubit Pauli operators for simplicity. For this case, the operation S^\dagger need not be applied at all, because S commutes with the time-evolution operator, $\exp(-it(H_1 - H_2^*)/\hbar)$, and with W and V .

We denote the measurement $\langle V^\dagger \otimes V^T \rangle$ made with $|g(\lambda)\rangle$ as $O_g(\lambda, t)$, to distinguish it from the thermal OTOC $O_{\text{th}}(\beta, t)$. The nonzero infidelity between $|g(\lambda)\rangle$ and $|\phi(\beta_0)\rangle$, for finite $\lambda \neq 0$, yields $O_g(\lambda, t) \neq O_{\text{th}}(\beta_0, t)$. Formally, the error is loosely bounded for all times t by [see Appendix C for proof]

$$\begin{aligned} |O_g(\lambda, t) - O_{\text{th}}(\beta_0, t)| &< 2\|V\|^2 D(|g(\lambda)\rangle, |\phi(\beta_0)\rangle) \\ &= 2\|V\|^2 \sqrt{1 - F(\beta_0, \lambda)} \end{aligned} \quad (12)$$

where $D(|g(\lambda)\rangle, |\phi(\beta_0)\rangle) = \sqrt{1 - F(\beta_0, \lambda)}$ is the trace distance between $|g(\lambda)\rangle$ and $|\phi(\beta_0)\rangle$, and $\|V\|$ is the spectral norm of V . In practice however, the error is much smaller at initial times, and grows with time.

The error at all times is significantly reduced by estimating a corrected OTOC given by

$$O_{\text{corr}}(\lambda, t) \equiv O_g(\lambda, t)/N_g(\lambda, t), \quad (13)$$

where N_g is obtained by performing the measurements with $W = 1$ in the prepared ground state $|g(\lambda)\rangle$. This ratio closely approximates $\tilde{O}_{\text{th}}(\beta_0, t) \equiv O_{\text{th}}(\beta_0, t)/|O_{\text{th}}(\beta_0, 0)|$.

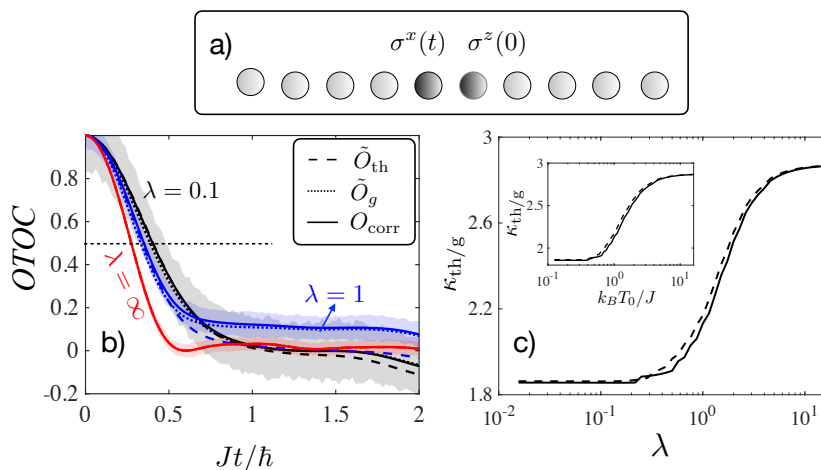


Figure 3. (a) A chain of 10 spins for which we calculate the OTOC for $W = \sigma_6^z$ and $V = \sigma_5^x$. (b) OTOCs $\tilde{O}_g(\lambda, t) = O_g(\lambda, t)/O_g(\lambda, t=0)$ (dashed), $\tilde{O}_{\text{th}}(\beta_0, t) = O_{\text{th}}(\beta_0, t)/O_{\text{th}}(\beta_0, t=0)$ (dotted), and $O_{\text{corr}}(\lambda, t) = O_g(\lambda, t)/N_g(\lambda, t)$ (solid), at three different couplings. Shaded areas indicate 1σ statistical error in O_{corr} from 1000 measurements of O_g and N_g at each time. The dashed, dotted, and solid curves coincide at $\lambda = \infty$ (red), but differ for the other two couplings. (c) The slope $\kappa = d\tilde{O}/dt$, for \tilde{O}_{th} at $\tilde{O}_{\text{th}} = 0.5$ (dashed), and for \tilde{O}_g at $\tilde{O}_g = 0.5$ (solid). The slope monotonically increases with coupling λ , and saturates at $\lambda \sim 10$. The inset displays κ as function of temperature $T_0 = T_0(\lambda)$, with $T_0(\lambda) = 1/\beta_0(\lambda)$ determined numerically by maximizing the overlap $F(\beta, \lambda)$ (see main text and Figure 2).

The intuitive reason for this is that the nonideality of the initial state, $|g(\lambda)\rangle \neq |\phi(\beta_0)\rangle$, drives similar dynamics in $N_g(\lambda, t)$ and $O_g(\lambda, t)$, and this dynamics is partially canceled in the ratio $O_{\text{corr}}(\lambda, t)$. Then, much of the remaining dynamics in $O_{\text{corr}}(\lambda, t)$ is only due to the scrambling of W . We note that this technique has been successfully applied in earlier works [56, 69, 86, 87] to mitigate errors in measuring the OTOC due to decoherence and noise sources. Other protocols also use qubit teleportation as a means to distinguish decay of OTOCs from genuine scrambling versus decay due to decoherence [57, 70, 73, 74].

4.1. Numerical results for the OTOC

In this section, we demonstrate that (a) $O_g(\lambda, t)$ approximates $O_{\text{th}}(\beta_0, t)$, which is the theoretical OTOC as defined in (1) for inverse temperature β_0 corresponding to the coupling λ , (b) the nontrivial temperature-dependence of $O_{\text{th}}(\beta_0, t)$ is captured well by choosing W and V as Pauli operators on adjacent spins, $W = \sigma_i^\mu$ and $V = \sigma_{i-1}^\nu$, and (c) errors due to non-ideal fidelity for finite $\lambda \neq 0$ are significantly reduced in $O_{\text{corr}}(\lambda, t)$ defined in (13).

Figure 3(b) plots the OTOCs at three different couplings, corresponding to different temperatures [see Figure 2], choosing $W = \sigma_6^z$, $V = \sigma_5^x$, and $n = 8$ as illustrated in Figure 3(a). Dotted lines correspond to $\tilde{O}_{\text{th}}(\beta_0, t) \equiv O_{\text{th}}(\beta_0, t)/O_{\text{th}}(\beta_0, 0)$, dashed lines to $\tilde{O}_g(\lambda, t) \equiv O_g(\lambda, t)/O_g(\lambda, 0)$, and solid lines to $O_{\text{corr}}(\lambda, t) \equiv O_g(\lambda, t)/N_g(\lambda, t)$. The curves start from an initial value of 1 and decay with time. There is good agreement

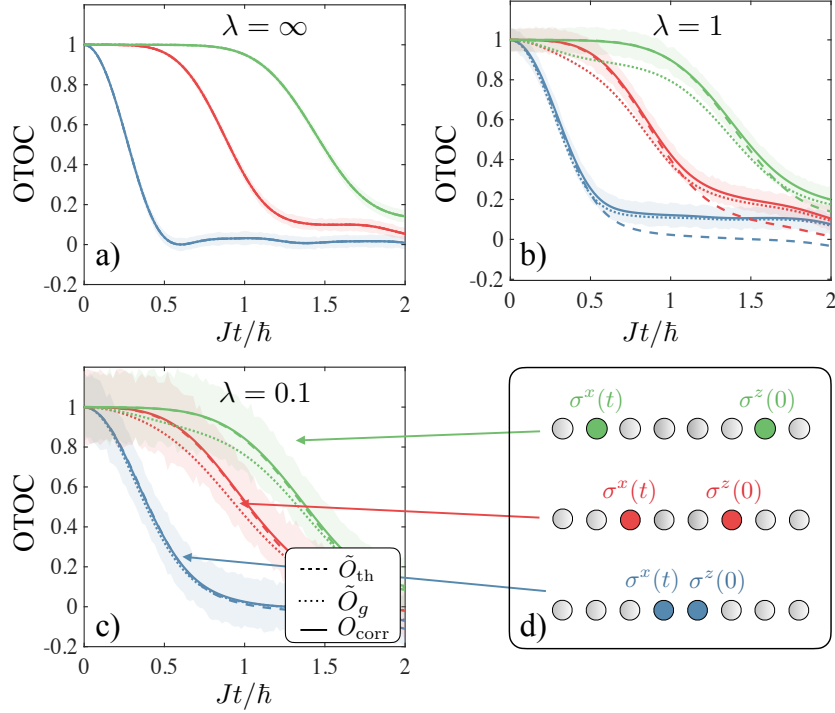


Figure 4. (a-c) OTOCs \tilde{O}_g (dotted), \tilde{O}_{th} (dashed), and O_{corr} (solid) versus time. Each panel considers a different coupling λ . The dotted, dashed, and solid curves coincide at $\lambda = \infty$ (panel a). (d) Choices of W and V in panels (a-c), and their color schemes. Blue lines in (a-c) correspond to $W = \sigma_3^z$ and $V = \sigma_4^x$, red lines to $W = \sigma_6^z$ and $V = \sigma_3^x$, and green lines to $W = \sigma_5^z$ and $V = \sigma_2^x$. $n = 8$ in all cases. Shaded areas indicate 1σ statistical error in O_{corr} from 1000 measurements of O_g and N_g at each time.

between them throughout most of the decay. The three curves agree exactly at $\lambda = \infty$ (red curves), but finite size effects and the non-ideality of the initial state for the other two couplings introduce a large disagreement between \tilde{O}_{th} and \tilde{O}_g at $Jt/\hbar \gtrsim 0.5$ and $Jt/\hbar \gtrsim 1$. As claimed earlier, the disagreement between \tilde{O}_{th} and O_{corr} is smaller than the disagreement between \tilde{O}_{th} and O_g . Shaded areas plot the 1σ shot noise from 1000 measurements. The overall scale of O_g decreases as temperature decreases, thereby increasing the shot noise. The shot noise increases with time for the same reason.

The OTOCs' decay rate is different at the three couplings in Figure 3(b). Figure 3(c) further illustrates this by plotting the slope κ of $\tilde{O}_{\text{th/g}}$ (solid/dashed) at $\tilde{O}_{\text{th/g}} = 0.5$. This slope monotonically increases with λ and saturates at $\lambda \sim 10$. The inset plots the slope versus T_0 . The fact that the slope, which is a measure of the rate of the OTOC's decay, depends on the state's temperature is a unique feature which has not been experimentally measured before. A key accomplishment of experimentally implementing our protocol would be measuring this temperature-dependence.

Figures 4(a-c) plot the OTOCs for different choices of W and V shown in Figure 4(d), and for different couplings, corresponding to different temperatures [see Figure 2], indicated at the top of each panel.

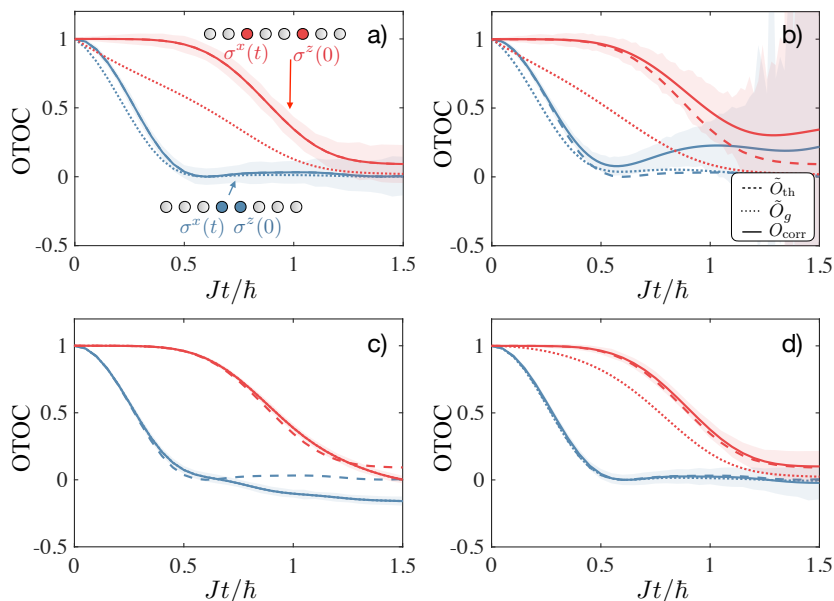


Figure 5. OTOCs \tilde{O}_g (dotted), \tilde{O}_{th} (dashed), and O_{corr} (solid) versus time, in the presence of four error sources. We set $\lambda = \infty$ and $n = 8$. (a) considers depolarization with $\gamma = J$. (b) considers local dephasing with $\gamma = J/4$. (c) considers interaction ϵH_{12} between the two legs during time evolution, with strength $\epsilon = 0.5$. (d) considers the two legs evolving with unequal Hamiltonians $(1 \pm \epsilon)H$, with $\epsilon = 0.2$. Blue lines correspond to $W = \sigma_5^z$ and $V = \sigma_4^x$, and red lines to $W = \sigma_6^z$ and $V = \sigma_3^x$, as shown in the two spin chains in (a). Dashed and solid lines completely overlap in (a). Dotted and solid lines completely overlap in (c). Shaded areas indicate 1σ statistical error in O_{corr} from 1000 measurements of O_g and N_g at each time.

\tilde{O}_{th} , \tilde{O}_g , and O_{corr} always agree at $\lambda = \infty$ [Figure 4(a)], since our protocol is exact in this case. The OTOC stays nearly constant at $\tilde{O}_g = 1$ for some time before the onset of decay. The time for which it remains nearly constant, $t \sim r/v_B$, is set by the distance r between W and V , and the butterfly velocity v_B [88–90]. This is because the measurement of $V^\dagger \otimes V^T$ at time t is affected only by the neighborhood where the Heisenberg operator $V^\dagger(t) \otimes V^T(t)$ has sufficient support, and this neighborhood grows linearly with time.

\tilde{O}_{th} and \tilde{O}_g disagree for finite $\lambda \neq 0$ [Figure 4(b-c)], and the error is larger when W and V are farther apart from each other. Specifically, \tilde{O}_g begins decreasing at $t = 0$ while \tilde{O}_{th} begins decaying at $t \sim r/v_B$ as explained above. The earlier onset of decay in \tilde{O}_g is because $|g(\lambda)\rangle$ evolves with time since it is not an eigenstate of $H_1 - H_2^*$. The spins in each leg get correlated with each other during this evolution, and consequently the correlation $V^\dagger \otimes V^T$ across the two legs gets weaker. Remarkably, O_{corr} has a much smaller error with \tilde{O}_{th} than the error between \tilde{O}_g and \tilde{O}_{th} .

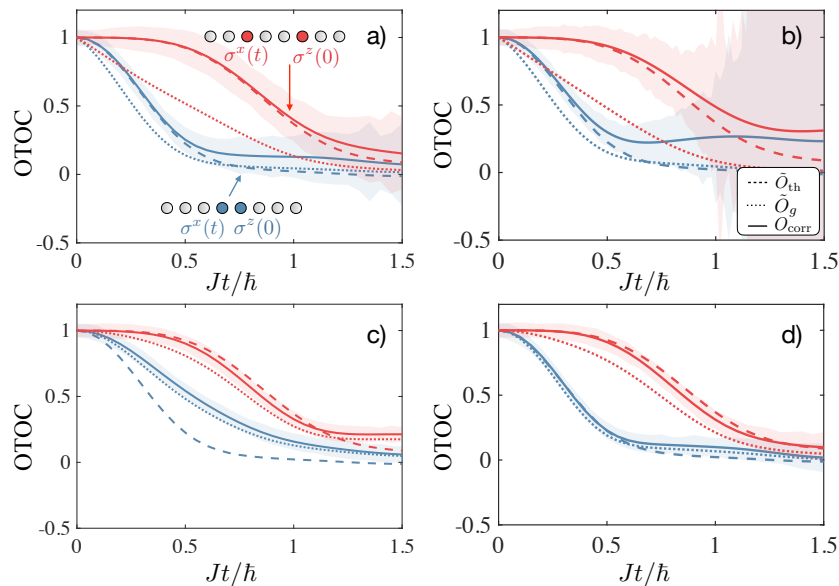


Figure 6. OTOCs \tilde{O}_g (dotted), \tilde{O}_{th} (dashed), and O_{corr} (solid) versus time, in the presence of four error sources. We set $\lambda = 1$ and $n = 8$. (a) considers depolarization with $\gamma = J$. (b) considers local dephasing with $\gamma = J/4$. (c) considers interaction ϵH_{12} between the two legs during time evolution, with strength $\epsilon = 0.5$. (d) considers the two legs evolving with unequal Hamiltonians $(1 \pm \epsilon)H$, with $\epsilon = 0.2$. Blue lines correspond to $W = \sigma_5^z$ and $V = \sigma_4^x$, and red lines to $W = \sigma_6^z$ and $V = \sigma_3^x$, as shown in the two spin chains in (a). Shaded areas indicate 1σ statistical error in O_{corr} from 1000 measurements of O_g and N_g at each time.

5. Robustness to experimental errors

Decoherence in the system during time evolution, or other sources of imperfections, can produce errors in \tilde{O}_g , even in the limits $\lambda = 0$ and $\lambda = \infty$ where our protocol is supposed to be exact. We consider a few different error mechanisms in this section. For the Hamiltonian we consider [(6)], we find in all cases except local dephasing that O_{corr} removes these errors at least partially and agrees well with \tilde{O}_{th} . Note that the bound derived for $|O_g - O_{\text{th}}|$ [(12)] only considers errors in the initial state, and is not valid for the error mechanisms in this section.

The first source of decoherence we consider is collective dephasing, caused by fluctuations in the global magnetic field. We model collective dephasing with the Lindblad equation

$$\hbar \partial_t \rho = -i[H_1 - H_2^*, \rho] - \gamma \left(S^z \rho S^z - \frac{1}{2} ((S^z)^2 \rho + \rho (S^z)^2) \right), \quad (14)$$

where we recall $S^z = \sum_{i=1}^{2n} \sigma_i^z$, and $\rho(\lambda, 0) = |g(\lambda)\rangle \langle g(\lambda)|$ for the normalization N_g and $\rho(\lambda, 0) = W |g(\lambda)\rangle \langle g(\lambda)| W^\dagger$ for O_g . Remarkably, N_g is completely robust to global dephasing, because $|g(\lambda)\rangle$ is an eigenstate of S^z with eigenvalue 0 for all λ , and $H_1 - H_2^*$ preserves S^z . Thus, the system always lies in a decoherence-free subspace and is insensitive to field fluctuations. O_g is also completely robust to global fluctuations

for any W that commutes with S^z , e.g., $W = \sigma_i^z$. A similar argument in the Heisenberg picture also implies that O_g is completely robust to collective dephasing if $V^\dagger \otimes V^T$ commutes with S^z , e.g., $V = \sigma_i^z$.

The second source of decoherence we consider is depolarization, caused by random collective spin flips along all directions. We model depolarization with the Lindblad equation

$$\hbar\partial_t\rho = -i[H_1 - H_2^*, \rho] - \gamma\left(\rho - \frac{1}{4^n}\right). \quad (15)$$

This equation has the solution

$$\rho(\lambda, t) = e^{-i(H_1 - H_2^*)t/\hbar}\rho e^{-i(H_1 - H_2^*)t/\hbar}e^{-\gamma t} + (1 - e^{-\gamma t})/4^n. \quad (16)$$

It is then straightforward to show that

$$\begin{aligned} N_g(\lambda, t; \gamma) &= e^{-\gamma t}N_g(\lambda, t; \gamma = 0), \\ O_g(\lambda, t; \gamma) &= e^{-\gamma t}O_g(\lambda, t; \gamma = 0). \end{aligned} \quad (17)$$

Our protocol is completely robust to depolarization as well, because the factor $e^{-\gamma t}$ in O_g and N_g cancel each other to give the correct value for O_{corr} .

Figures 5(a) and 6(a) illustrate this robustness to depolarization, at $\lambda = \infty$ and $\lambda = 1$, and $\gamma = J$ in both cases. At $\lambda = \infty$, $O_{\text{corr}} = \tilde{O}_{\text{th}}$ exactly. At $\lambda = 1$, $O_{\text{corr}} \neq \tilde{O}_{\text{th}}$ because of the finite infidelity of $|g(\lambda)\rangle$ with $|\phi(\beta_0)\rangle$, but no additional errors are introduced by depolarization. The only effect of depolarization on O_{corr} in both cases is that the shot noise is larger than the one in the case of $\gamma = 0$. This is because the two factors O_g and N_g in the ratio $O_{\text{corr}} = O_g/N_g$ are separately measured in experiment, and each factor has a smaller value with depolarization than without. The smaller values lead to a larger shot noise that increases exponentially with γ .

The third source of decoherence we consider is local dephasing, caused by magnetic field fluctuations on each spin. We model local dephasing with the Lindblad equation

$$\hbar\partial_t\rho = -i[H_1 - H_2^*, \rho] - \gamma\sum_{i=1}^{2n}(\sigma_i^z\rho\sigma_i^z - \rho), \quad (18)$$

Figures 5(b) and 6(b) plot \tilde{O}_{th} (dashed), \tilde{O}_g (dotted) and O_{corr} (solid) at $\lambda = \infty$ and $\lambda = 1$, and $\gamma = J/4$ in both cases. We see a large disagreement between \tilde{O}_{th} and \tilde{O}_g , and a smaller but significant disagreement \tilde{O}_{th} and O_{corr} .

The fourth and fifth error mechanisms we consider are caused by imperfections in the unitary evolution. In Figures 5(c) and 6(c), we consider the case that the coupling between the ladder's two legs is not completely turned off during the time evolution, but there is a remnant coupling ϵH_{12} with $\epsilon = 0.5$. In Figures 5(d) and 6(d), we consider the case that the ladder's two legs have different intra-leg interaction strengths, i.e. they evolve with $(1 - \epsilon)H_1 - (1 + \epsilon)H_2^*$. We set $\epsilon = 0.2$. At $\lambda = \infty$, O_{corr} agrees well with \tilde{O}_{th} for both the error mechanisms. The agreement between them is poorer at $\lambda = 1$.

The next error mechanism we consider is due to errors in the initial state, arising from a finite temperature of the parent system. This error is relevant when the parent

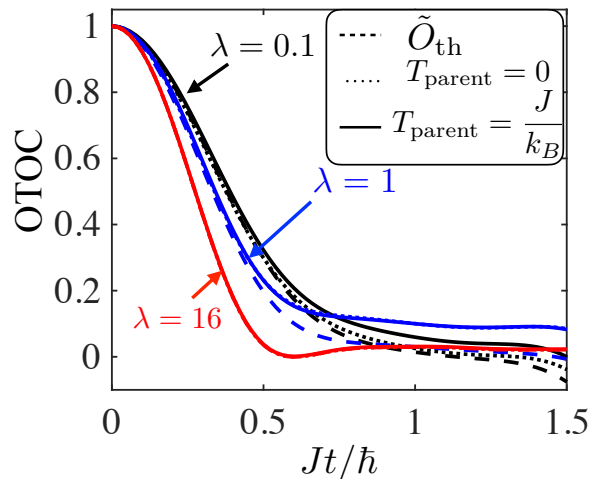


Figure 7. OTOCs versus time, when the parent state is at a finite temperature $T_{\text{parent}} = J$, i.e. the initial state is $\rho \propto \exp(-H_{\text{parent}}(\lambda)/T_{\text{parent}})$. Dashed, dotted, and solid lines plot \tilde{O}_{th} , O_{corr} for $T_{\text{parent}} = 0$, and O_{corr} for $T_{\text{parent}} = J$. The colors correspond to the couplings λ indicated in the figure. All three red curves nearly indistinguishable, and the blue dotted and solid lines are also nearly indistinguishable from each other.

system is not prepared in the ground state $|g(\lambda)\rangle$, but at a finite temperature T_{parent} , i.e. the initial state is $\rho \propto \exp(-H_{\text{parent}}(\lambda)/k_B T_{\text{parent}})$. Physically, since $H_{\text{parent}}(\lambda)$ has a gap $\Delta \propto \lambda$ [see Figure 2], the initial state would have a large overlap with $|g(\lambda)\rangle$ if $T_{\text{parent}} \ll \lambda J$. Moreover, we expect that our correction protocol will mitigate this error, just as it did for the nonzero infidelity of $|g(\lambda)\rangle$ with $|\phi(\beta)\rangle$. We show evidence for this claim in Figure 7, where we plot the OTOCs for the case the parent system has a temperature $T_{\text{parent}} = J/k_B$. We find that the agreement between O_{corr} and \tilde{O}_{th} at $T_{\text{parent}} = J/k_B$ is comparable to the agreement at $T_{\text{parent}} = 0$. We further analyse the error $|O_{\text{corr}} - \tilde{O}_{\text{th}}|$ in Appendix D.

In addition to mitigating errors due to imperfections in the initial state ($F(\beta_0, \lambda) < 1$), and due to decoherence during time evolution, O_{corr} also corrects errors in measurement. This is the sixth source of error we consider. If the ideal probability to measure $V^\dagger \otimes V^T$ as $(\pm 1, \pm 1)$ after time evolution is $P_{\pm 1, \pm 1}$, and the error probability for each measurement is x , then the ideal and incorrect expectation values of $V^\dagger \otimes V^T$ are respectively

$$\begin{aligned} \langle V^\dagger \otimes V^T \rangle_{\text{ideal}} &= \sum_{\sigma_1, \sigma_2 = \pm 1} \sigma_1 \sigma_2 P_{\sigma_1, \sigma_2}, \\ \langle V^\dagger \otimes V^T \rangle_{\text{incorrect}} &= \sum_{\sigma_1, \sigma_2 = \pm 1} \sigma_1 \sigma_2 \left((1-x)^2 P_{\sigma_1, \sigma_2} + x(1-x)(P_{\sigma_1, -\sigma_2} + P_{-\sigma_1, \sigma_2}) \right. \\ &\quad \left. + x^2 P_{-\sigma_1, -\sigma_2} \right). \end{aligned} \quad (19)$$

Simplifying the second line of (19) gives

$$\langle V^\dagger \otimes V^T \rangle_{\text{incorrect}} = (1 - 2x)^2 \langle V^\dagger \otimes V^T \rangle_{\text{ideal}}. \quad (20)$$

Thus, readout errors rescale the ideal expectation value by $(1 - 2x)^2$, in both the factors O_g and N_g . The ratio O_{corr} completely removes readout errors.

6. Connections to earlier works

At infinite temperature, our proposed method is related to two protocols presented earlier in Refs. [56, 57]. These have been experimentally implemented to measure the infinite-temperature OTOC in trapped ion quantum simulators [69, 70] and superconducting circuits [73, 74].

In Refs. [56, 69], a protocol which employed statistical correlations of randomized measurements to measure the infinite-temperature OTOC was described and realized. Based on correlating separate (sequential) experimental runs, which are initialized in randomized product states and evolved forward in time, it requires only single instances of the n -qubit quantum system. The key idea is to rewrite $O_{\text{th}}(\beta = 0, t)$ as

$$O_{\text{th}}(\beta = 0, t) = \text{tr}(\text{SWAP} \cdot W^\dagger V^\dagger(t) W \otimes V(t)) / 2^n. \quad (21)$$

with $\text{SWAP} = \sum_{\vec{x}, \vec{x}'} |\vec{x}\rangle \langle \vec{x}'| \otimes |\vec{x}'\rangle \langle \vec{x}|$ where the sum runs over all computational basis states $|\vec{x}\rangle$, parametrized by bit strings $\vec{x} = (x_i)_{i=1, \dots, n}$ with $x_i = 0, 1$. As shown in [56], the crux of the method consists in effectively realizing the *two-copy observable* $\text{SWAP}/4^n$ as an average of randomized initial product states *on single copies* which can be prepared in separate (sequential) experimental runs,

$$\frac{\text{SWAP}}{4^n} = \sum_{\vec{x}} (-2)^{-|\vec{x}|} \overline{(u |\vec{x}\rangle \langle \vec{x}| u^\dagger) \otimes (u |\vec{0}\rangle \langle \vec{0}| u^\dagger)}. \quad (22)$$

Here, $|\vec{x}| \equiv \sum_i x_i$ and the overline denotes the average over local random unitaries $u = \bigotimes_{i=1, \dots, n} u_i$, with u_i sampled independently for each spin from unitary 2 designs [56]. The OTOC is then measured by evolving the system, initialized in the randomized product states $(u |\vec{x}\rangle \langle \vec{x}| u^\dagger)$ forward in time and measure the operators $W^\dagger V^\dagger(t) W$ and $V(t)$, respectively. We note that in practice, the sum in (22) can be truncated to obtain a rapidly converging series of modified OTOCs [56].

The SWAP operator is not positive semi-definite, i.e. it is not a density matrix describing a quantum state. The connection to our protocol can however be understood by mathematically applying a transpose operation to qubits $[n + 1, 2n]$ in (22). This yields [91, 92]

$$\frac{|\text{tfd}(\beta = 0)\rangle \langle \text{tfd}(\beta = 0)|}{2^n} = \sum_{\vec{x}} (-2)^{-|\vec{x}|} \overline{(u |\vec{x}\rangle \langle \vec{x}| u^\dagger) \otimes (u^* |\vec{0}\rangle \langle \vec{0}| u^T)}, \quad (23)$$

where u^T and u^* are respectively the transpose and complex conjugate of u . The infinite-temperature state $|\text{tfd}(\beta = 0)\rangle \langle \text{tfd}(\beta = 0)|$ can thus be effectively realized as an average over correlated random initial states, prepared by applying u and u^* to bit strings $|\vec{x}\rangle$ and $|\vec{0}\rangle$ in two separate (sequential) runs of the experiment [91, 92].

In contrast to the above protocol, we propose in the present work to physically realize $|\text{tfd}(\beta = 0)\rangle \langle \text{tfd}(\beta = 0)|$ as a pure quantum state on two copies of the systems ($2n$

qubits). As described in Section 2, the OTOC is then measured by evolving the first copy with H and the second copy with $-H^*$, to measure the operator $W^\dagger V^\dagger(t)W \otimes (V(t))^T$, with

$$\begin{aligned} (V(t))^T &= \exp(-iH^T t) V^T \exp(iH^T t) \\ &= \exp(-iH^* t) V^T \exp(iH^* t). \end{aligned} \quad (24)$$

In summary, the quantum protocol for OTOC measurements presented in this work requires twice the number of qubits as the randomized protocol, and requires fine-tuning to realize time evolution with $-H^* = R^\dagger H R$. It can however be readily extended to arbitrary finite temperatures, by preparing finite temperature TFDs $|\text{tfd}(\beta)\rangle \langle \text{tfd}(\beta)|$, and also requires fewer measurements than the randomized protocol in general.

A previous quantum protocol to measure the infinite-temperature OTOC was implemented in [70] and [73, 74], following [57]. There, the authors prepared $2n$ qubits in $|\text{tfd}(\beta = 0)\rangle$, and one additional independent qubit. Then they evolved the two sets of n qubits independently, similar to our method, and finally measured two qubits in the Bell basis. Because of this measurement basis, they could extract the sum of OTOCs $\sum_{W,V} \text{tr}(W^\dagger V^\dagger(t)WV(t)) / (16 \cdot 2^n)$, where the sum runs over the three Pauli operators and the identity for a spin. The sum of these OTOCs is related to the probability that the initially independent qubit teleported from its initial location to a final location. Thus, our protocols are identical at $\beta = 0$, except for the presence of the initially independent qubit and choice of the final measurement basis.

We also briefly comment that a previous work [61] proposed a method to measure a *differently* regularized finite-temperature OTOC [see Appendix A]. In this work, the authors sample $2n$ qubits from thermal ensembles and measures overlap between the qubits after coupling to an ancilla and time evolution. Ref. [56] proposed a method to measure a symmetrized variant of the finite-temperature OTOC [see Appendix A] at high temperature. In this protocol, the finite-temperature correction to the infinite-temperature OTOC is obtained via statistical correlations between randomized measurements with global random unitaries. Both the above protocols do not require sign reversal of the Hamiltonian. It is also possible to measure the thermal OTOC by sampling states from a thermal ensemble, and making weak measurements together with forward and backward time evolution of the system [63]. All these protocols yield an OTOC that is regularized differently from the OTOC we consider in this paper [see Appendix Appendix A].

7. Discussion & Conclusion

We described an experimentally feasible protocol to measure a system's finite-temperature out-of-time-ordered correlation, which is a quantitative probe of the nature of information scrambling. Our method utilizes earlier ideas to prepare the TFD ($|\text{tfd}(\beta)\rangle$) [18, 19], and measure the thermal OTOC from $|\text{tfd}(\beta)\rangle$ [75]. It is geared towards analog quantum simulators with a Hamiltonian respecting particle-hole

symmetry and satisfying the ETH, but can also be realized in other analog systems as well as digital quantum simulators. As an example, we considered the long-ranged XX model that was recently realized in [13], and our protocol can be extended to other models. We access the finite temperature state as one half of $|\text{tfd}(\beta)\rangle$ which is related to the ground state of a local Hamiltonian acting on two copies of the system. For the example we considered, the ground state on two copies of the system well-approximated the desired state for moderate system sizes. In a digital quantum simulator, $|\text{tfd}(\beta)\rangle$ may be prepared variationally for small systems [76, 77]. The OTOC can be obtained by measuring local correlations between two halves of the system, after applying a local perturbation and evolving the two halves independently.

Our protocol works accurately at $T = \infty$ and $T = 0$, and works reasonably well in the vicinity of these temperatures. The errors in our protocol are largest near $\lambda = 1$. We described a correction procedure to mitigate the errors in our protocol, which arise from non-ideal fidelity of the prepared initial state with the thermofield double state. We found that this correction procedure yields values for OTOCs that agree well with the exact normalized thermal OTOCs at short times, and mitigate errors due to imperfect initial state, and thus allows us to extract useful physics, e.g. the temperature-dependence of the nearest-neighbor OTOCs' decay. Further, we found that the same normalization procedure also mitigated errors due to decoherence at short times. While our protocol captures short-time dynamics of the OTOCs, it does not capture their steady-state behavior.

There are several directions that future works could explore. They could investigate how to improve the preparation of the TFD for measuring thermal OTOCs as well as a variety of other applications, for example by adding more terms to the inter-chain coupling Hamiltonian. Alternatively, one could use variational techniques in various fashions, either directly as a variational circuit to prepare the TFD as in Ref. [76], or using variational ansätze to find the parent Hamiltonian, similar to recent works which adopted variational techniques for the opposite problem of finding the modular Hamiltonian [80]. It will be useful to develop other correction methods that complement our protocol to distinguish measured decay of the OTOC due to scrambling from measured decay due to decoherence or imperfect initial state. Protocols to measure the other regularizations also need to be developed and realized in experiment.

We discussed connections between our method at $T = \infty$ and methods adopted in earlier experiments [69, 70, 73, 74]. Applying our method in finite temperature systems with a maximally scrambling Hamiltonian will provide a rigorous test for analytical predictions about information scrambling in these systems [25, 26]. Our method can be straightforwardly applied in systems where the Hamiltonian's sign can be reversed in experiment explicitly, and in systems with a particle-hole symmetric Hamiltonian where explicitly reversing the Hamiltonian's sign will not be necessary. New algorithms are needed for systems where neither of these are true.

Our method goes beyond the paradigm of the infinite temperature OTOC measured in experiments earlier [69, 70, 73, 74], and could lead to the first experimental

measurement of the finite-temperature OTOC. The TFD has been of interest in quantum gravity in the context of wormhole teleportation [93–95]. Recently, this teleportation through wormhole has been shown to be thought of as information scrambling in a coupled chain of qubits [96]. Our work can set a useful benchmark via the measurement of thermal OTOCs for such ‘quantum gravity in lab’ ideas [97–99].

Acknowledgments

Work in Innsbruck was supported by the innovation program under the Grant Agreement No. 731473 (FWF QuantERA via QTFLAG I03769), from the Austrian Science Foundation (FWF, P 32597 N) and by the Simons Collaboration on UltraQuantum Matter, which is a grant from the Simons Foundation (651440, P.Z.). A.E. acknowledges funding by the German National Academy of Sciences Leopoldina under the grant number LPDS 2021-02.

We thank Ana Maria Rey and Murray Holland for a careful reading of the manuscript. We thank Norbert Linke, Alaina Green, and Benoit Vermersch for valuable discussions and comments on the manuscript.

References

- [1] Rainer Blatt and Christian F Roos. Quantum simulations with trapped ions. *Nat. Phys.*, 8(4):277–284, 2012.
- [2] Chris Monroe, Wes C Campbell, Lu-Ming Duan, Z-X Gong, Alexey V Gorshkov, P W Hess, R Islam, K Kim, Norbert M Linke, Guido Pagano, et al. Programmable quantum simulations of spin systems with trapped ions. *Rev. Mod. Phys.*, 93(2):025001, 2021.
- [3] Christian Gross and Immanuel Bloch. Quantum simulations with ultracold atoms in optical lattices. *Science*, 357(6355):995–1001, 2017.
- [4] Antoine Browaeys and Thierry Lahaye. Many-body physics with individually controlled rydberg atoms. *Nat. Phys.*, 16(2):132–142, 2020.
- [5] Morten Kjaergaard, Mollie E Schwartz, Jochen Braumüller, Philip Krantz, Joel I-J Wang, Simon Gustavsson, and William D Oliver. Superconducting qubits: Current state of play. *Annu. Rev. Condens. Matter Phys.*, 11:369–395, 2020.
- [6] Lieven M K Vandersypen and Isaac L Chuang. Nmr techniques for quantum control and computation. *Rev. Mod. Phys.*, 76(4):1037, 2005.
- [7] Jonathan A Jones. Quantum computing with nmr. *Prog. NMR Spectrosc.*, 59:91–120, 2011.
- [8] Ivan Oliveira, Roberto Sarthour Jr, Tito Bonagamba, Eduardo Azevedo, and Jair C C Freitas. *NMR quantum information processing*. Elsevier (New York), 2011.
- [9] Hui Sun, Bing Yang, Han-Yi Wang, Zhao-Yu Zhou, Guo-Xian Su, Han-Ning Dai, Zhen-Sheng Yuan, and Jian-Wei Pan. Realization of a bosonic antiferromagnet. *arXiv preprint arXiv:2009.01426*, 2020.
- [10] Peter T Brown, Debayan Mitra, Elmer Guardado-Sanchez, Reza Nourafkan, Alexis Reymbaut, Charles-David Hébert, Simon Bergeron, A-MS Tremblay, Jure Kokalj, David A Huse, et al. Bad metallic transport in a cold atom fermi-hubbard system. *Science*, 363(6425):379–382, 2019.
- [11] Matthew A Nichols, Lawrence W Cheuk, Melih Okan, Thomas R Hartke, Enrique Mendez, T Senthil, Ehsan Khatami, Hao Zhang, and Martin W Zwierlein. Spin transport in a mott insulator of ultracold fermions. *Science*, 363(6425):383–387, 2019.

- [12] Anton Mazurenko, Christie S Chiu, Geoffrey Ji, Maxwell F Parsons, Márton Kanász-Nagy, Richard Schmidt, Fabian Grusdt, Eugene Demler, Daniel Greif, and Markus Greiner. A cold-atom fermi–hubbard antiferromagnet. *Nature*, 545(7655):462–466, 2017.
- [13] Sylvain de Léséleuc, Vincent Lienhard, Pascal Scholl, Daniel Barredo, Sebastian Weber, Nicolai Lang, Hans Peter Büchler, Thierry Lahaye, and Antoine Browaeys. Observation of a symmetry-protected topological phase of interacting bosons with rydberg atoms. *Science*, 365(6455):775–780, 2019.
- [14] Pascal Scholl, Michael Schuler, Hannah J Williams, Alexander A Eberharter, Daniel Barredo, Kai-Niklas Schymik, Vincent Lienhard, Louis-Paul Henry, Thomas C Lang, Thierry Lahaye, Andreas M Läuchli, and Antoine Browaeys. Programmable quantum simulation of 2d antiferromagnets with hundreds of rydberg atoms. *arXiv preprint arXiv:2012.12268*, 2020.
- [15] Sepehr Ebadi, Tout T Wang, Harry Levine, Alexander Keesling, Giulia Semeghini, Ahmed Omran, Dolev Bluvstein, Rhine Samajdar, Hannes Pichler, Wen Wei Ho, et al. Quantum phases of matter on a 256-atom programmable quantum simulator. *arXiv preprint arXiv:2012.12281*, 2020.
- [16] Giulia Semeghini, Harry Levine, Alexander Keesling, Sepehr Ebadi, Tout T Wang, Dolev Bluvstein, Ruben Verresen, Hannes Pichler, Marcin Kalinowski, Rhine Samajdar, et al. Probing topological spin liquids on a programmable quantum simulator. *arXiv preprint arXiv:2104.04119*, 2021.
- [17] Christian Kokail, Christine Maier, Rick van Bijnen, Tiff Brydges, Manoj K Joshi, Petar Jurcevic, Christine A Muschik, Pietro Silvi, Rainer Blatt, Christian F Roos, and Peter Zoller. Self-verifying variational quantum simulation of lattice models. *Nature*, 569(7756):355–360, 2019.
- [18] William Cottrell, Ben Freivogel, Diego M Hofman, and Sagar F Lokhande. How to build the thermofield double state. *J. High Ener. Phys.*, 2019(2):58, 2019.
- [19] Juan Maldacena and Xiao-Liang Qi. Eternal traversable wormhole. *arXiv preprint arXiv:1804.00491*, 2018.
- [20] Brian Swingle. Unscrambling the physics of out-of-time-order correlators. *Nat. Phys.*, 14(10):988–990, 2018.
- [21] Akram Touil and Sebastian Deffner. Quantum scrambling and the growth of mutual information. *Quantum Sci. Technol.*, 5(3):035005, 2020.
- [22] Eiki Iyoda and Takahiro Sagawa. Scrambling of quantum information in quantum many-body systems. *Phys. Rev. A*, 97(4):042330, 2018.
- [23] Nima Lashkari, Douglas Stanford, Matthew Hastings, Tobias Osborne, and Patrick Hayden. Towards the fast scrambling conjecture. *J. High Energy Phys.*, 2013(4):22, 2013.
- [24] Stephen H Shenker and Douglas Stanford. Multiple shocks. *J. High Energy Phys.*, 2014(12):46, 2014.
- [25] Juan Maldacena, Stephen H Shenker, and Douglas Stanford. A bound on chaos. *J. High Energy Phys.*, 2016(8):106, 2016.
- [26] Chaitanya Murthy and Mark Srednicki. Bounds on chaos from the eigenstate thermalization hypothesis. *Phys. Rev. Lett.*, 123(23):230606, 2019.
- [27] Daniel A. Roberts and Douglas Stanford. Diagnosing chaos using four-point functions in two-dimensional conformal field theory. *Phys. Rev. Lett.*, 115:131603, Sep 2015.
- [28] Pavan Hosur, Xiao-Liang Qi, Daniel A Roberts, and Beni Yoshida. Chaos in quantum channels. *J. High Energy Phys.*, 2016(2):4, 2016.
- [29] Xiao Chen, Tianci Zhou, David A Huse, and Eduardo Fradkin. Out-of-time-order correlations in many-body localized and thermal phases. *Annalen der Physik*, 529(7):1600332, 2017.
- [30] Koji Hashimoto, Keiju Murata, and Ryosuke Yoshii. Out-of-time-order correlators in quantum mechanics. *J. High Energy Phys.*, 2017(10):138, 2017.
- [31] C. W. von Keyserlingk, Tibor Rakovszky, Frank Pollmann, and S. L. Sondhi. Operator hydrodynamics, otocs, and entanglement growth in systems without conservation laws. *Phys. Rev. X*, 8:021013, Apr 2018.

- [32] Yunxiang Liao and Victor Galitski. Nonlinear sigma model approach to many-body quantum chaos: Regularized and unregularized out-of-time-ordered correlators. *Phys. Rev. B*, 98:205124, Nov 2018.
- [33] Juan Maldacena and Douglas Stanford. Remarks on the sachdev-ye-kitaev model. *Phys. Rev. D*, 94:106002, Nov 2016.
- [34] Aavishkar A. Patel, Debanjan Chowdhury, Subir Sachdev, and Brian Swingle. Quantum butterfly effect in weakly interacting diffusive metals. *Phys. Rev. X*, 7:031047, Sep 2017.
- [35] Annabelle Bohrdt, Christian B Mendl, Manuel Endres, and Michael Knap. Scrambling and thermalization in a diffusive quantum many-body system. *New J. Phys.*, 19(6):063001, 2017.
- [36] Cheng-Ju Lin and Olexei I Motrunich. Out-of-time-ordered correlators in a quantum ising chain. *Phys. Rev. B*, 97(14):144304, 2018.
- [37] Ceren B Dağ and L-M Duan. Detection of out-of-time-order correlators and information scrambling in cold atoms: Ladder-xx model. *Phys. Rev. A*, 99(5):052322, 2019.
- [38] Tibor Rakovszky, Frank Pollmann, and C W Von Keyserlingk. Diffusive hydrodynamics of out-of-time-ordered correlators with charge conservation. *Phys. Rev. X*, 8(3):031058, 2018.
- [39] Vedika Khemani, Ashvin Vishwanath, and David A Huse. Operator spreading and the emergence of dissipative hydrodynamics under unitary evolution with conservation laws. *Phys. Rev. X*, 8(3):031057, 2018.
- [40] Markus J Klug, Mathias S Scheurer, and Jörg Schmalian. Hierarchy of information scrambling, thermalization, and hydrodynamic flow in graphene. *Phys. Rev. B*, 98(4):045102, 2018.
- [41] Douglas Stanford. Many-body chaos at weak coupling. *J. High Energy Phys.*, 2016(10):9, 2016.
- [42] Ron Belyansky, Przemyslaw Bienias, Yaroslav A. Kharkov, Alexey V. Gorshkov, and Brian Swingle. A minimal model for fast scrambling. *Phys. Rev. Lett.*, 125:130601, 2020.
- [43] Zehan Li, Sayan Choudhury, and W. Vincent Liu. Fast scrambling without appealing to holographic duality. *Phys. Rev. Res.*, 2:043399, Dec 2020.
- [44] Sagar Vijay and Ashvin Vishwanath. Finite-temperature scrambling of a random hamiltonian. *arXiv preprint arXiv: 1803.08483*.
- [45] Bryce Kobrin, Zhenbin Yang, Gregory D. Kahanamoku-Meyer, Christopher T. Olund, Joel E. Moore, Douglas Stanford, and Norman Y. Yao. Many-body chaos in the sachdev-ye-kitaev model. *Phys. Rev. Lett.*, 126:030602, Jan 2021.
- [46] Paul Romatschke. Quantum mechanical out-of-time-ordered-correlators for the anharmonic (quartic) oscillator. *J. High Energy Phys.*, 2021(1):30, 2021.
- [47] Robert J Lewis-Swan, Sean R Muleady, and Ana Maria Rey. Detecting out-of-time-order correlations via quasiadiabatic echoes as a tool to reveal quantum coherence in equilibrium quantum phase transitions. *Phys. Rev. Lett.*, 125(24):240605, 2020.
- [48] Xinfang Nie, Bo-Bo Wei, Xi Chen, Ze Zhang, Xiuzhu Zhao, Chudan Qiu, Yu Tian, Yunlan Ji, Tao Xin, Dawei Lu, and Jun Li. Experimental observation of equilibrium and dynamical quantum phase transitions via out-of-time-ordered correlators. *Phys. Rev. Lett.*, 124(25):250601, 2020.
- [49] Ceren B Dağ, Kai Sun, and Luming M Duan. Detection of quantum phases via out-of-time-order correlators. *Phys. Rev. Lett.*, 123(14):140602, 2019.
- [50] Ceren B Dağ, Luming M Duan, and Kai Sun. Topologically induced prescrambling and dynamical detection of topological phase transitions at infinite temperature. *Phys. Rev. B*, 101(10):104415, 2020.
- [51] Bo-Bo Wei, Gaoyong Sun, and Myung-Joong Hwang. Dynamical scaling laws of out-of-time-ordered correlators. *Phys. Rev. B*, 100(19):195107, 2019.
- [52] Zheng-Hang Sun, Jia-Qi Cai, Qi-Cheng Tang, Yong Hu, and Heng Fan. Out-of-time-order correlators and quantum phase transitions in the rabi and dicke models. *Ann. Phys. (Leipzig)*, 532(4):1900270, 2020.
- [53] Qian Wang and Francisco Pérez-Bernal. Probing an excited-state quantum phase transition in a quantum many-body system via an out-of-time-order correlator. *Phys. Rev. A*, 100(6):062113, 2019.

- [54] Markus Heyl, Frank Pollmann, and Balázs Dóra. Detecting equilibrium and dynamical quantum phase transitions in ising chains via out-of-time-ordered correlators. *Phys. Rev. Lett.*, 121(1):016801, 2018.
- [55] Huitao Shen, Pengfei Zhang, Ruihua Fan, and Hui Zhai. Out-of-time-order correlation at a quantum phase transition. *Phys. Rev. B*, 96(5):054503, 2017.
- [56] Benoît Vermersch, Andreas Elben, Lukas M Sieberer, Norman Y Yao, and Peter Zoller. Probing scrambling using statistical correlations between randomized measurements. *Phys. Rev. X*, 9(2):021061, 2019.
- [57] Beni Yoshida and Norman Y Yao. Disentangling scrambling and decoherence via quantum teleportation. *Phys. Rev. X*, 9(1):011006, 2019.
- [58] Brian Swingle, Gregory Bentsen, Monika Schleier-Smith, and Patrick Hayden. Measuring the scrambling of quantum information. *Phys. Rev. A*, 94(4):040302(R), 2016.
- [59] Guanyu Zhu, Mohammad Hafezi, and Tarun Grover. Measurement of many-body chaos using a quantum clock. *Phys. Rev. A*, 94(6):062329, 2016.
- [60] Sreeram P G, Naga Dileep Varikuti, and Vaibhav Madhok. Exponential speedup in measuring out-of-time-ordered correlators with a single bit of quantum information. *arXiv preprint arXiv:2009.03415*, 2020.
- [61] Norman Y Yao, Fabian Grusdt, Brian Swingle, Mikhail D Lukin, Dan M Stamper-Kurn, Joel E Moore, and Eugene A Demler. Interferometric approach to probing fast scrambling. *arXiv preprint arXiv:1607.01801*, 2016.
- [62] Nicole YungerHalpern. Jarzynski-like equality for the out-of-time-ordered correlator. *Phys. Rev. A*, 95(1):012120, 2017.
- [63] Justin Dressel, José Raúl González Alonso, Mordecai Waegell, and Nicole Yunger Halpern. Strengthening weak measurements of qubit out-of-time-order correlators. *Phys. Rev. A*, 98(1):012132, 2018.
- [64] Jun Li, Ruihua Fan, Hengyan Wang, Bingtian Ye, Bei Zeng, Hui Zhai, Xinhua Peng, and Jiangfeng Du. Measuring out-of-time-order correlators on a nuclear magnetic resonance quantum simulator. *Phys. Rev. X*, 7(3):031011, 2017.
- [65] Ken Xuan Wei, Chandrasekhar Ramanathan, and Paola Cappellaro. Exploring localization in nuclear spin chains. *Phys. Rev. Lett.*, 120(7):070501, 2018.
- [66] Xinfang Nie, Ze Zhang, Xiuzhu Zhao, Tao Xin, Dawei Lu, and Jun Li. Detecting scrambling via statistical correlations between randomized measurements on an nmr quantum simulator. *arXiv preprint arXiv:1903.12237*, 2019.
- [67] S Pegahan, I Arakelyan, and J E Thomas. Energy-resolved information scrambling in energy-space lattices. *Phys. Rev. Lett.*, 126(7):070601, 2021.
- [68] Martin Gärttner, Justin G Bohnet, Arghavan Safavi-Naini, Michael L Wall, John J Bollinger, and Ana Maria Rey. Measuring out-of-time-order correlations and multiple quantum spectra in a trapped-ion quantum magnet. *Nat. Phys.*, 13(8):781–786, 2017.
- [69] Manoj K Joshi, Andreas Elben, Benoît Vermersch, Tiff Brydges, Christine Maier, Peter Zoller, Rainer Blatt, and Christian F Roos. Quantum information scrambling in a trapped-ion quantum simulator with tunable range interactions. *Phys. Rev. Lett.*, 124:240505, 2020.
- [70] Kevin A Landsman, Caroline Figgatt, Thomas Schuster, Norbert M Linke, Beni Yoshida, Norman Yao, and Christopher Monroe. Verified quantum information scrambling. *Nature*, 567(7746):61–65, 2019.
- [71] Xiao Mi, Pedram Roushan, Chris Quintana, Salvatore Mandra, Jeffrey Marshall, Charles Neill, Frank Arute, Kunal Arya, Juan Atalaya, Ryan Babbush, et al. Information scrambling in computationally complex quantum circuits. *arXiv preprint arXiv:2101.08870*, 2021.
- [72] Jochen Braumüller, Amir H Karamlou, Yariv Yanay, Bharath Kannan, David Kim, Morten Kjaergaard, Alexander Melville, Bethany M Niedzielski, Youngkyu Sung, Antti Vepsäläinen, et al. Probing quantum information propagation with out-of-time-ordered correlators. *arXiv preprint arXiv:2102.11751*, 2021.

- [73] Machiel S Blok, V V Ramasesh, Thomas Schuster, K O'Brien, JM Kreikebaum, D Dahlen, A Morvan, Beni Yoshida, Norman Y Yao, and Irfan Siddiqi. Quantum information scrambling on a superconducting qutrit processor. *Phys. Rev. X*, 11(2):021010, 2021.
- [74] J.-H Wang, T.-Q Cai, X.-Y Han, Y.-W Ma, Z.-L Wang, Z.-H Bao, Y Li, H.-Y Wang, H.-Y Zhang, L.-Y Sun, Y.-K Wu, Y.-P Song, and Lu-Ming Duan. Verifying quantum information scrambling dynamics in a fully controllable superconducting quantum simulator. *arXiv preprint arXiv:2112.11204*, 2021.
- [75] Étienne Lantagne-Hurtubise, Stephan Plugge, Oguzhan Can, and Marcel Franz. Diagnosing quantum chaos in many-body systems using entanglement as a resource. *Phys. Rev. Res.*, 2(1):013254, 2020.
- [76] Daiwei Zhu, Sonika Johri, Norbert M Linke, K A Landsman, C Huerta Alderete, Nhung H Nguyen, A Y Matsuura, T H Hsieh, and Chris Monroe. Generation of thermofield double states and critical ground states with a quantum computer. *Proceedings of the National Academy of Sciences*, 117(41):25402–25406, 2020.
- [77] Akhil Francis, Daiwei Zhu, C. Huerta Alderete, Sonika Johri, Xiao Xiao, Jim K. Freericks, Chris Monroe, Norbert M. Linke, and A. F. Kemper. Many body thermodynamics on quantum computers via partition function zeros. *arXiv preprint arXiv:2009.04648*, 2020.
- [78] Ingo Peschel and Ming-Chiang Chung. On the relation between entanglement and subsystem hamiltonians. *EPL (Europhys. Lett.)*, 96(5):50006, 2011.
- [79] Andreas M Läuchli and John Schliemann. Entanglement spectra of coupled $s=1/2$ spin chains in a ladder geometry. *Phys. Rev. B*, 85(5):054403, 2012.
- [80] Christian Kokail, Bhuvanesh Sundar, Torsten V Zache, Andreas Elben, Benoît Vermersch, Marcello Dalmonte, Rick van Bijnen, and Peter Zoller. Quantum variational learning of the entanglement hamiltonian. *arXiv preprint arXiv:2105.04317*, 2021.
- [81] Mahdiah Pourjafarabadi, Hanieh Najafzadeh, Mohammad-Sadegh Vaezi, and Abolhassan Vaezi. Entanglement hamiltonian of interacting systems: Local temperature approximation and beyond. *Phys. Rev. Res.*, 3(1):013217, 2021.
- [82] Joseph J Bisognano and Eyvind H Wichmann. On the duality condition for a hermitian scalar field. *J. Math. Phys.*, 16(4):985–1007, 1975.
- [83] Joseph J Bisognano and Eyvind H Wichmann. On the duality condition for quantum fields. *J. Math. Phys.*, 17(3):303–321, 1976.
- [84] John Cardy and Erik Tonni. Entanglement hamiltonians in two-dimensional conformal field theory. *J. Stat. Mech. Theory Exp.*, 2016(12):123103, 2016.
- [85] Xiao-Liang Qi, Hosho Katsura, and Andreas WW Ludwig. General relationship between the entanglement spectrum and the edge state spectrum of topological quantum states. *Phys. Rev. Lett.*, 108(19):196402, 2012.
- [86] Brian Swingle and Nicole YungerHalpern. Resilience of scrambling measurements. *Phys. Rev. A*, 97(6):062113, 2018.
- [87] Yong-Liang Zhang, Yichen Huang, and Xie Chen. Information scrambling in chaotic systems with dissipation. *Phys. Rev. B*, 99(1):014303, 2019.
- [88] Daniel A Roberts and Brian Swingle. Lieb-robinson and the butterfly effect in quantum field theories. *Phys. Rev. Lett.*, 117(9):091602, 2016.
- [89] Daniel A Roberts, Douglas Stanford, and Leonard Susskind. Localized shocks. *J. High Energy Phys.*, 2015(3):1–27, 2015.
- [90] Márk Mezei and Douglas Stanford. On entanglement spreading in chaotic systems. *J. High Energy Phys.*, 2017(5):1–24, 2017.
- [91] J. Watrous. *The Theory of Quantum Information*. Cambridge University Press (Cambridge), 2018.
- [92] Andreas Elben, Jinlong Yu, Guanyu Zhu, Mohammad Hafezi, Frank Pollmann, Peter Zoller, and Benoît Vermersch. Many-body topological invariants from randomized measurements in synthetic quantum matter. *Sci. Adv.*, 6(15):eaaz3666, Apr 2020.

- [93] Juan Maldacena. Eternal black hole. *JHEP*, 04:021, 2003.
- [94] Juan Maldacena, Douglas Stanford, and Zhenbin Yang. Diving into traversable wormholes. *Fortsch. Phys.*, 65(5), may 2017.
- [95] Ping Gao, Daniel Louis Jafferis, and Aron C. Wall. Traversable wormholes via a double trace deformation. *J. High Energy Phys.*, 2017(12), dec 2017.
- [96] Thomas Schuster, Bryce Kobrin, Ping Gao, Iris Cong, Emil T. Khabiboulline, Norbert M. Linke, Mikhail D. Lukin, Christopher Monroe, Beni Yoshida, and Norman Y. Yao. Many-body quantum teleportation via operator spreading in the traversable wormhole protocol. *arXiv preprint arXiv: 2102.00010*.
- [97] Adam R. Brown, Hrant Gharibyan, Stefan Leichenauer, Henry W. Lin, Sepehr Nezami, Grant Salton, Leonard Susskind, Brian Swingle, and Michael Walter. Quantum gravity in the lab: Teleportation by size and traversable wormholes. *arXiv preprint arXiv: 1911.06314*.
- [98] Sepehr Nezami, Henry W. Lin, Adam R. Brown, Hrant Gharibyan, Stefan Leichenauer, Grant Salton, Leonard Susskind, Brian Swingle, and Michael Walter. Quantum gravity in the lab: Teleportation by size and traversable wormholes, part ii. *arXiv preprint arXiv: 2102.01064*.
- [99] Arpan Bhattacharyya, Lata Kh Joshi, and Bhuvanesh Sundar. Quantum information scrambling: From holography to quantum simulators. *arXiv preprint arXiv:2111.11945*, 2021.
- [100] Michael A Nielsen and Isaac Chuang. *Quantum computation and quantum information*. Cambridge University Press (New York), 2002.

Appendix A. Different definitions of thermal OTOC

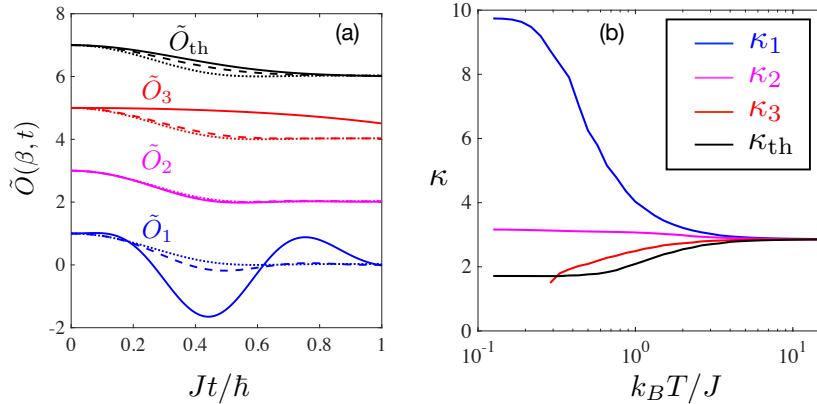


Figure A1. (a) Normalized OTOCs $\tilde{O}_{1/2/3/th}(\beta, t)$ and (b) their rates of decay, where we define $\tilde{O}(t) = O(t)/O(0)$. (a) Blue curves plot $\tilde{O}_1(\beta, t)$, magenta curves are $\tilde{O}_2(\beta, t)$, red curves are $\tilde{O}_3(\beta, t)$, and black curves are $\tilde{O}_{th}(\beta, t)$. Solid, dashed, and dotted lines correspond to $k_B T/J = 1/8, 1, 8$ respectively. The curves corresponding to \tilde{O}_2 , \tilde{O}_3 , and \tilde{O}_{th} are shifted from one another vertically by 2, 4, and 6, respectively for clarity. Each curve's unshifted value at $t = 0$ is 1, due to their normalization. (b) The slope of $\tilde{O}(\beta, t)$ at $\tilde{O}(\beta, t) = 0.5$. The different OTOCs exhibit very different slopes, and even show different trends with temperature. The curves are unshifted in (b).

Researchers have used various definitions of the thermal OTOC in the literature. These are:

$$O_1(\beta, t) = \frac{\text{tr} \left(y^2 W^\dagger V^\dagger(t) y^2 W V(t) \right)}{\text{tr} \left(e^{-\beta H} \right)},$$

$$\begin{aligned}
 O_2(\beta, t) &= \frac{\text{tr}(y^4 W^\dagger V^\dagger(t) W V(t))}{\text{tr}(e^{-\beta H})}, \\
 O_3(\beta, t) &= \frac{\text{tr}(y W^\dagger y V^\dagger(t) y W y V(t))}{\text{tr}(e^{-\beta H})}, \\
 O_{\text{th}}(\beta, t) &= \frac{\text{tr}(y^2 W^\dagger V^\dagger(t) W y^2 V(t))}{\text{tr}(e^{-\beta H})},
 \end{aligned} \tag{A.1}$$

where $y = e^{-\beta H/4}$. The definition in the last line is used by us in this paper. The above definitions typically show different behaviors from one another for non-maximally-scrambling Hamiltonians at finite temperature. They converge to the same value for $\beta = 0$. Refs. [61] described a quantum algorithm, based on sampling thermal states, to measure $O_2(\beta, t)$, and [75] proposed to measure $O_{\text{th}}(\beta, t)$ and $O_1(\beta, t)$ using the TFD. Algorithms to experimentally measure $O_3(\beta, t)$ at arbitrary temperature have not been developed. Here, we investigate their behaviors for the Hamiltonian in (6).

Figure A1(a) plots $\tilde{O}_{1/2/3/\text{th}}(\beta, t)$ for $W = \sigma_6^z$ and $V = \sigma_5^x$ as in the main text, at different temperatures, where we define $\tilde{O}(t) = O(t)/O(0)$. All the four kinds of OTOC decay initially with time. But their decay rates are very different from one another. Further, the decay's temperature-dependence is different for the four definitions. While the decay gets steeper as temperature increases for O_{th} and O_3 , it gets less steep for O_1 and is nearly temperature-independent for O_2 . As before, we compute and plot the curves' slopes at $\tilde{O} = 1/2$ in Figure A1(b). The slope κ increases with temperature for O_{th} (Figure 2 and black curve in Figure A1(b)) and O_3 (red curve), decreases with temperature for O_1 (blue curve), and is nearly constant for O_2 (pink curve).

We gain an understanding of the magnitude of the unnormalized OTOCs from Figure A2, which plots $O_{1/2/3/\text{th}/g}(\beta, t=0)$ versus $k_B T/J$. For O_g , we choose the inter-chain coupling λ which gives maximum overlap between $|g(\lambda)\rangle$ and $|\text{tfd}(\beta)\rangle$, as in the main text. The magnitude of the OTOC is $O(\beta, t) = \tilde{O}(\beta, t)O(\beta, t=0)$. We find that $O_2(\beta, t=0) = 1$. This is because $W^\dagger V^\dagger W V = 1$ and $\text{tr}(y^4)/\text{tr}(e^{-\beta H}) = 1$. The other four are less than 1 for all finite T , and increase with temperature.

Why these different OTOCs, all of which have been used in the literature, have different values and decay at different rates, and what aspects of information scrambling they capture or miss, are intriguing questions for future exploration.

Appendix B. TFD for $n = 2$

Here, we show that $|g(\lambda)\rangle = |\phi(\beta_0)\rangle$ for $n = 2$. The ground state of $H_{\text{parent}}(\lambda)$ is

$$\begin{aligned}
 |g(\lambda)\rangle &= -\frac{\lambda}{2\sqrt{1+\lambda^2}} (|\uparrow\uparrow\rangle |\downarrow\downarrow\rangle + |\downarrow\downarrow\rangle |\uparrow\uparrow\rangle) \\
 &\quad -\frac{1}{2\sqrt{1+\lambda^2}} (|\uparrow\downarrow\rangle |\uparrow\downarrow\rangle + |\downarrow\uparrow\rangle |\downarrow\uparrow\rangle) \\
 &\quad +\frac{1}{2} (|\uparrow\downarrow\rangle |\downarrow\uparrow\rangle + |\downarrow\uparrow\rangle |\uparrow\downarrow\rangle).
 \end{aligned} \tag{B.1}$$

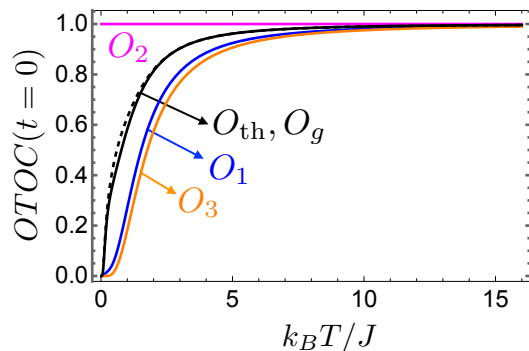


Figure A2. Initial ($t=0$) values of the unnormalized OTOCs defined in Eq. (A.1) and in the main text, namely O_1 (blue), O_2 (magenta), O_3 (orange), O_{th} (black), and O_g (black dashed) versus temperature. The unnormalized $O_2(\beta, t=0)$ is always 1, while the other four increase with temperature. For this system size ($n=10$), $O_{\text{th}}(t=0)$ is very close in magnitude to $O_g(t=0)$.

Similarly,

$$\begin{aligned}
 |\phi(\beta)\rangle = & -\frac{1}{2 \cosh \beta} (|\uparrow\uparrow\rangle |\downarrow\downarrow\rangle + |\downarrow\downarrow\rangle |\uparrow\uparrow\rangle) \\
 & -\frac{\tanh \beta}{2} (|\uparrow\downarrow\rangle |\uparrow\downarrow\rangle + |\downarrow\uparrow\rangle |\downarrow\uparrow\rangle) \\
 & +\frac{1}{2} (|\uparrow\downarrow\rangle |\downarrow\uparrow\rangle + |\downarrow\uparrow\rangle |\uparrow\downarrow\rangle). \tag{B.2}
 \end{aligned}$$

A straightforward comparison gives $|g(\lambda)\rangle = |\phi(\beta_0)\rangle$ when $\lambda = 1/\sinh \beta_0$.

Appendix C. Upper bound for errors due to the initial state

For any two states ρ and σ , the difference in the expectation value of any operator O can be upper bounded as follows. First, we expand O in its eigen basis $\{|o_\mu\rangle\}$,

$$\langle O \rangle_\rho - \langle O \rangle_\sigma = \sum_\mu o_\mu \langle o_\mu | \rho - \sigma | o_\mu \rangle. \tag{C.1}$$

Using the triangle sum rule,

$$\langle O \rangle_\rho - \langle O \rangle_\sigma \leq \sum_\mu |o_\mu| \langle o_\mu | \rho - \sigma | o_\mu \rangle. \tag{C.2}$$

Then, using $|o_\mu| \leq \|O\|$, with $\|O\|$ being the spectral norm of O , and the definition of the trace distance $D(\rho, \sigma)$, we get

$$\langle O \rangle_\rho - \langle O \rangle_\sigma \leq 2\|O\|D(\rho, \sigma). \tag{C.3}$$

The operator measured in our protocol is $O = V \otimes V^T$, which has spectral norm $\|V\|^2$. This proves the first line in (12), with $\rho = |g(\lambda)\rangle \langle g(\lambda)|$ and $\sigma = |\phi(\beta_0)\rangle \langle \phi(\beta_0)|$. These states are pure states, and a standard property [100] for pure states leads to the second line in (12). The bound is valid for all times, since the spectral norm of a Heisenberg operator is constant with time evolution.

Appendix D. Errors in our protocol

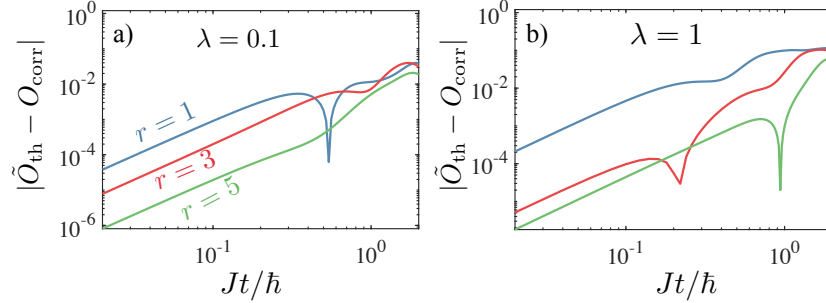


Figure D1. The error $|\tilde{O}_{\text{th}} - O_{\text{corr}}|$ versus Jt/\hbar at (a) $\lambda = 0.1$, and (b) $\lambda = 1$, for the same operators and distances considered in Fig. 4. The error $|\tilde{O}_{\text{th}} - O_{\text{corr}}|$ grows with time, and decreases with r at a fixed time.

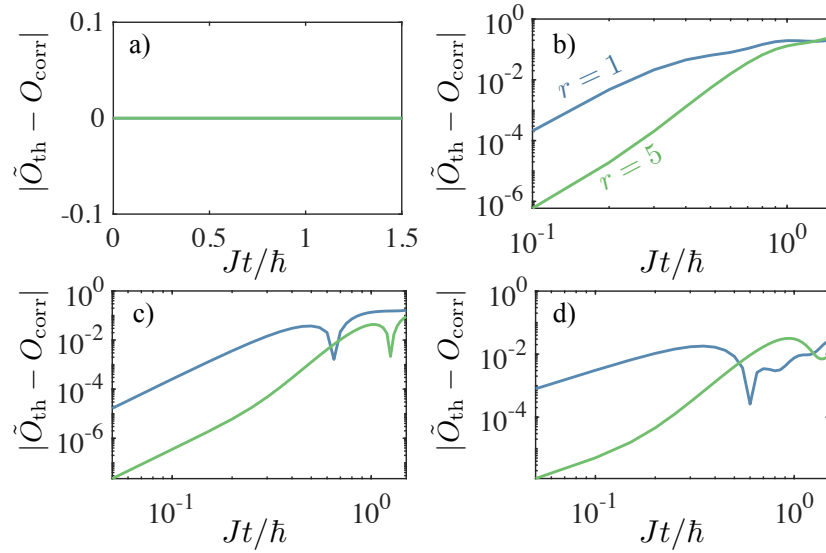


Figure D2. The error $|\tilde{O}_{\text{th}} - O_{\text{corr}}|$ versus Jt/\hbar at $\lambda = \infty$, with the four sources of decoherence considered in Fig. 5. Each panel plots $|\tilde{O}_{\text{th}} - O_{\text{corr}}|$ for $r = 1$ (blue) and $r = 5$ (green), and shows that the error grows with time, and decreases with r at a fixed time.

In Figures 3-7, we plotted the normalized OTOCs \tilde{O}_g and \tilde{O}_{th} , and the corrected OTOC O_{corr} . We observed from the figures that $|\tilde{O}_{\text{th}} - O_{\text{corr}}| < |\tilde{O}_{\text{th}} - \tilde{O}_g|$. Here, we analyze the error $|\tilde{O}_{\text{th}} - O_{\text{corr}}|$ in more detail.

Figure D1 plots $|\tilde{O}_{\text{th}} - O_{\text{corr}}|$ versus time, for two couplings $\lambda = 0.1$ and $\lambda = 1$, corresponding to the Figures 4(b) and (c). We find that the errors increases $\propto t^2$, at short times. We also find that the error decreases with distance at a fixed time, supporting our reason in the main text for correcting O_g with N_g .

Figure D2 plots $|\tilde{O}_{\text{th}} - O_{\text{corr}}|$ versus time at $\lambda = \infty$, in the presence of the four sources of decoherence considered in Fig. 5. Figure D3 plots the errors versus time at

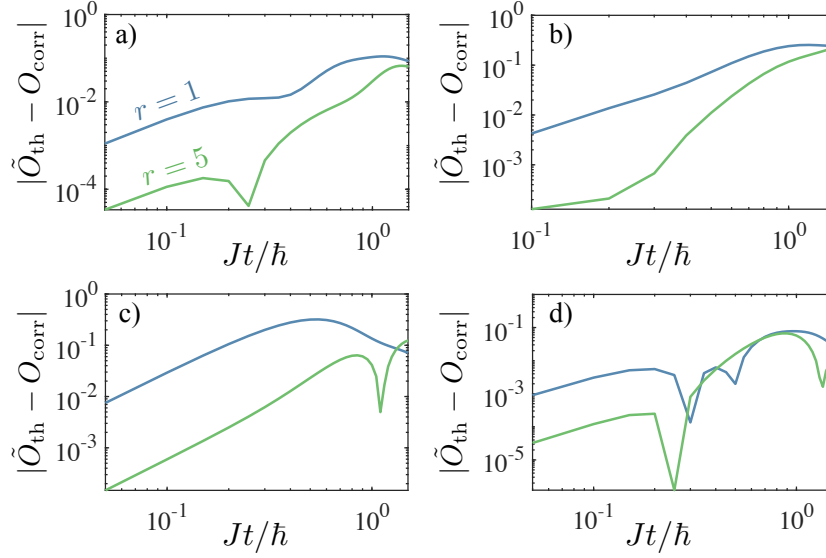


Figure D3. The error $|\tilde{O}_{\text{th}} - O_{\text{corr}}|$ versus Jt/\hbar at $\lambda = 1$, with the four sources of decoherence considered in Fig. 6. Each panel plots $|\tilde{O}_{\text{th}} - O_{\text{corr}}|$ for $r = 1$ (blue) and $r = 5$ (green), and shows that the error grows with time, and decreases with r at a fixed time.

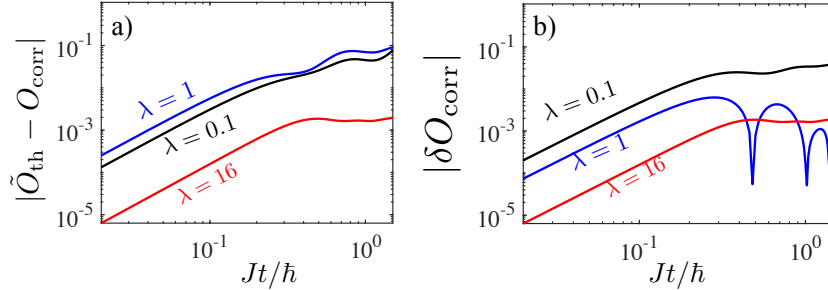


Figure D4. (a) The error $|\tilde{O}_{\text{th}} - O_{\text{corr}}|$ versus Jt/\hbar , where $O_{\text{corr}} = O(\lambda)/N(\lambda)$ is the corrected OTOC for the case where the parent system's initial state is at a finite temperature, $T_{\text{parent}} = J/k_B$. The error at a given time is largest for $\lambda = 1$, corresponding to the case that the initial state's fidelity with $|\phi(\beta_0)\rangle$ is lowest. (b) The difference between O_{corr} at $T_{\text{parent}} = 0$ and at $T_{\text{parent}} = J/k_B$. The error at a given time is largest for $\lambda = 0.1$, corresponding to the case that the parent Hamiltonian's gap Δ is the smallest.

$\lambda = 1$, with the same sources of decoherence. Similar to Fig. D1, we find in both cases that the error increases with time, and decreases with distance.

Figure D4 plots the error in the OTOC due to a finite temperature parent system, in two ways. In panel (a), we consider that the parent system is at a temperature $T_{\text{parent}} = J/k_B$, and plot the difference between the corrected OTOC and \tilde{O}_{th} . Among the three coupling strengths λ , this error is largest at $\lambda = 1$, mainly because the error is largest here even if the parent system is at zero temperature. In panel (b), we again consider that the parent system is at a temperature $T_{\text{parent}} = J/k_B$, but plot the difference between the OTOC measured in this state and the OTOC measured from the

zero-temperature parent state $|g(\lambda)\rangle$. Here, the error is largest when $\lambda = 0.1$, since the energy gap is the smallest for this case.